

REPEATED IMAGING OF MASSIVE BLACK HOLE BINARY ORBITS WITH MILLIMETER INTERFEROMETRY: MEASURING BLACK HOLE MASSES AND THE HUBBLE CONSTANT

DANIEL J. D’ORAZIO AND ABRAHAM LOEB

Department of Astronomy, Harvard University, 60 Garden Street Cambridge, MA 01238, USA

Draft Version November 5, 2018

ABSTRACT

Very long baseline interferometry (VLBI) at millimeter (mm) wavelengths is being employed to resolve event-horizon scale structure of the environment surrounding the Milky-Way black hole, at an angular resolution of a few tens of micro-arcseconds. The same approach could also resolve the orbital separation of a population of massive black hole binaries (MBHBs). Modeling the inspiral of binaries due to gravitational wave emission and gas and requiring binary orbital periods of less than 10 years, we estimate that there may exist ~ 100 resolvable MBHBs that are bright enough to be observed by mm-wavelength VLBI instruments over the entire sky, at redshifts $z \lesssim 0.5$. We propose to search for these resolvable MBHBs by identifying binaries with the required orbital separations from periodic quasar light curves identified in optical and near-IR surveys. These periodic-light-curve candidates can be followed up with radio observations to determine their promise for observation with VLBI at mm wavelengths. VLBI observations over the timescale of a binary orbit can allow unprecedented precision in the measurement of the binary mass, to within 30%. In combination with an independent binary mass measurement, VLBI observation would allow a novel $\mathcal{O}(10\%)$ measurement of the Hubble constant, independent from those currently proposed and employed.

1. INTRODUCTION

The merger of galaxies harboring massive black holes (MBHs [Kormendy and Richstone 1995](#); [Kauffmann and Haehnelt 2000](#); [Ferrearese and Ford 2005](#); [Kormendy and Ho 2013](#)) can lead to the formation of a compact massive black hole binary (MBHB) at the center of the newly formed galaxy ([Colpi and Dotti 2011](#)). For moderate MBH mass ratios ($\gtrsim 1:100$), dynamical friction can bring the MBHs together on the galactic dynamical timescale to form a hard binary with orbital separation of order parsecs (pc) (*e.g.* [Callegari et al. 2011](#); [Mayer 2013](#); [Dosopoulou and Antonini 2016](#)). Dynamical friction becomes inefficient at hardening the binary further at smaller orbital separations and alternative mechanisms for removing binary angular momentum and energy must be employed if the binary is to shrink to $\lesssim 0.01$ pc separations, where gravitational radiation will bring the binary to coalescence (*e.g.* [Begelman et al. 1980](#); [Merritt and Milosavljević 2005](#)).

Multiple mechanisms are capable of shrinking the binary orbital separation through this intervening stage, solving the so-called final-parsec problem ([Milosavljević and Merritt 2003](#)). Possible solutions include interaction of the binary with a gas disk ([Gould and Rix 2000](#); [Armitage and Natarajan 2002](#)) (for recent work see [Tang et al. 2017](#), and references therein), a massive perturber ([Goicovic et al. 2016](#)), or non-axisymmetric stellar distributions that allow a high interaction rate between stars and the binary (see [Gualandris et al. 2017](#), and references therein). However, to truly understand the mechanisms that drive MBHBs to merge in galactic nuclei, we must find observational tracers of the MBHB population, probing different stages of MBHB evolution. Based on reliable tracers of the MBHB population, the relative fraction of MBHBs at different orbital separations can be translated into the rates at which the binaries are driven together during these stages, and hence elucidate the mechanisms driving orbital decay (see, *e.g.*, [Haiman et al. 2009](#)).

These observational tracers naturally fall into the realm of multi-messenger astronomy. The earliest stages of MBHB formation, where the MBHs have not yet hardened into a binary, have been captured by direct electromagnetic (EM) imaging; two distinct active galactic nuclei with projected separations of 10’s to 1000’s of pc have been identified in radio, optical, and X-ray wavelengths ([Komossa 2006](#); [Rodríguez et al. 2006](#); [Burke-Spolaor 2011](#); [Fabbiano et al. 2011](#); [Dotti et al. 2012](#); [Civano et al. 2012](#); [Blecha et al. 2013](#); [Comerford et al. 2013](#); [Woo et al. 2014](#)). Low frequency gravitational radiation will probe the final stages of a MBHB’s life. Particularly, the stochastic background of gravitational waves detectable by the Pulsar Timing Arrays (PTAs) ([Lommen 2012](#); [Manchester and IPTA 2013](#); [McLaughlin 2013](#); [Kramer and Champion 2013](#); [Hobbs 2013](#); [Shannon et al. 2015](#)), will be sensitive to environmental effects determining the binary eccentricity and lifetime at \sim nHz orbital frequencies ([Kelley et al. 2017a](#)), probing the late inspiral of the most massive MBHBs.

The early, dynamical-friction-driven, and late, gravitational-radiation-driven phases of MBHB evolution are separated by the sub-pc orbital separation regime. At sub-pc orbital separations, it is likely that gas will accompany the MBHB (*e.g.* [Barnes and Hernquist 1996](#); [Barnes 2002](#)), not only aiding in resolution of the final-pc problem, but also providing the potential for bright EM signatures. However, identification of an EM signature with a compact MBHB must surmount the obstacle of disentangling signatures of an accreting MBHB from those of a single, accreting MBH. Finding unique EM identifiers of accreting, compact MBHBs has been the subject of numerous theoretical studies and corresponding observational searches. Possible signatures could arise from emission line dynamics (*e.g.*, [Shen and Loeb 2010](#); [Tsalmantza et al. 2011](#); [Bogdanović et al. 2009a](#); [Eracleous et al. 2012](#); [McKernan et al. 2013](#); [Decarli et al. 2013](#); [Shen et al. 2013](#); [Liu et al. 2014a, 2016](#)), tidal disruptions by a binary (*e.g.*, [Liu et al. 2009](#); [Stone and Loeb 2011](#); [Coughlin et al. 2017](#)), peculiar jet morphology

(e.g., Gower *et al.* 1982; Roos *et al.* 1993; Merritt and Ekers 2002; Zier and Biermann 2002; Romero *et al.* 2000; Kun *et al.* 2014, 2015; Kulkarni and Loeb 2016), orbital motion of an unresolved radio core observed with VLBI (Sudou *et al.* 2003, similar in goal to the ideas discussed here), or periodic emission and lensing events from quasars (Hayasaki and Mineshige 2008; Haiman *et al.* 2009; D’Orazio *et al.* 2013, 2015a; Farris *et al.* 2014; D’Orazio and Di Stefano 2017). Observational searches motivated by these studies have identified a number of individual MBHB candidates (Bogdanović *et al.* 2009b; Valtonen *et al.* 2008; Liu *et al.* 2014b; Graham *et al.* 2015a; Li *et al.* 2017), and recently, time domain searches for periodically varying quasars have identified ~ 140 MBHB candidates (Graham *et al.* 2015b; Charisi *et al.* 2016).

In order to use the growing population of MBHB candidates to investigate the drivers of MBHB evolution, further vetting of these candidates must be employed. For this to happen, new ways of identifying compact MBHBs, in conjunction with existing methods, must be developed. In this work we suggest the use of very long baseline interferometry (VLBI) at millimeter (mm) wavelengths to directly image the sky-projected orbital path of sub-pc separation MBHBs.

The outline of this paper is as follows. In Section 2 we present our criteria for tracking a MBHB orbit with VLBI. In Section 3 we present our calculation of the population of resolvable MBHBs and the resulting gravitational wave background due to this population. We present results in Section 4. In Section 4.1 we present our main results while Sections 4.2 and 4.3 provide a detailed analysis of the dependence of our results on model parameters (the reader primarily interested in the main results and implications may wish to skip Sections 4.2 and 4.3). In Section 5 we discuss the application of MBHB imaging to inferring the MBHB population, measuring the binary mass, and measuring the Hubble constant. In Section 6 we conclude.

2. IMAGING THE ORBIT OF A COMPACT MBHB

To image a MBHB orbit, we require that the binary orbital separation be i) larger than the minimum spatial resolution, ii) larger than the size of the emission region at the observing wavelength, and iii) both binary components be bright enough to be detectable independently, or that one component be bright and a calibrator source be nearby. We additionally impose that the binary orbital period be shorter than some maximum baseline timescale, P_{base} . By observing an entire orbit, we ensure that the binary nature of the source can be determined.

The first criterion can be met by mm-wavelength VLBI. VLBI experiments with maximum baselines the size of the Earth can reach diffraction limited resolutions on the order of $20\mu\text{as}$ when observing in $\lesssim\text{mm}$ wavelengths, and can reach sub-diffraction limited, down to $4\mu\text{as}$, resolutions using novel image reconstruction techniques (Akiyama *et al.* 2017a,b).¹ Astrometric tracking of a source can reach $1\mu\text{as}$ precision (Broderick *et al.* 2011). At 1 Gpc, a $10\mu\text{as}$ resolution corresponds to a physical binary orbital separation of 0.05pc and an orbital period of only 10 years for the most massive, $10^{10}M_{\odot}$, binaries. Hence the first criteria can be satisfied because radio-loud active galactic nuclei (AGN), which

may harbor close MBHBs, are also bright at mm and sub-mm wavelengths (e.g. Elvis *et al.* 1994).

To determine the validity of the second criterion, we estimate the size of the mm-wavelength emission region. Binaries for which this region is smaller than the separation will be viable targets for sub-mm VLBI imaging, otherwise the photosphere of the mm-emission region could mask the resolvable binary components or emanate from a region in a jet that is larger than the orbital separation. While emission regions that are larger than the binary orbital separation may still provide evidence for a binary via photometric variability or periodically changing geometry, they are possibly more complicated than the case of two distinguishable sources envisioned here.

Observationally, we can probe the size of the mm- to sub-mm emission region from variability measurements. Specifically, if the emission region is smaller than the binary separation, then in the most conservative case, causality requires that the light-travel distance over the duration of the shortest mm-variability timescales be smaller than the binary orbital separation,

$$\frac{c\Delta t_{\text{var}}^{\text{min}}}{(1+z)} \leq \theta_{\text{min}} D_A(z) \leq \left(\frac{\sqrt{GM}P_{\text{base}}}{2\pi(1+z)} \right)^{2/3}, \quad (1)$$

where the middle term is the smallest possible binary separation and the rightmost term is the largest binary separation for maximum allowed binary orbital period P_{base} . $D_A(z)$ is the angular diameter distance of the MBHB at redshift z .

Equation (1) requires that the observed mm-variability timescales satisfy $\Delta t_{\text{var}}^{\text{min}} \lesssim 1 \text{ day}$ ($\theta_{\text{min}}/1\mu\text{as}$) to resolve all possible MBHBs at $z \geq 0.02$ or $\Delta t_{\text{var}}^{\text{min}} \lesssim 54 \text{ days}$ $M_9^{1/3} P_{10}^{2/3}$ to resolve only the longest period, and most common (see next section) MBHBs at $z > 0.02$. Here M_9 is the total binary mass in units of $10^9 M_{\odot}$ and P_{10} is the maximum baseline period in units of 10 years.

Recent studies have employed the SMA calibrator database to characterize AGN variability in the sub-mm regime (Strom *et al.* 2010; Bower *et al.* 2015). They quantified the variability timescale by the damped random walk correlation timescale (MacLeod *et al.* 2010), finding that sub-mm variability of these brightest sources has characteristic timescales of $\sim 1 - 1000$ days. Notably, Bower *et al.* (2015) find that the low-luminosity AGN (LLAGN) exhibit shorter timescale variability than other blazars and AGN in the SMA calibrator sample. Furthermore, the characteristic timescale for variability of these sources appears to track a multiple of the MBH innermost stable circular orbit (ISCO), suggesting that mm-emission from LLAGN tracks the regions very close to the MBH.

That the mm-emission from LLAGN tracks event horizon scales is consistent with standard models for synchrotron emission from jets (Blandford and Königl 1979). In these models, the BH launches a jet and the mm-emission is generated by synchrotron radiation at shocks along the length of the jet. There is a smallest distance along the length of the jet from which optically thin, bright synchrotron radiation can be emitted. This minimum size scales with the bolometric jet luminosity. Because the jet is launched from a small region that is bound to the BH, the mm-emission will necessarily track the BH orbit, regardless of its size compared to the Roche radius. Hence, the size of the mm-emission region need not be truncated close to the BH for VLBI-orbit tracking to be vi-

¹ This fact is a leading driver behind the Event Horizon Telescope, which is currently being employed to resolve Schwarzschild-radius scale structure of the environment surrounding the Milky-Way black hole (Doeleman *et al.* 2008).

able. Rather, because we wish to consider systems for which the mm-emission regions emanating from each BH are clearly distinguishable, we compare the size of the emission region with the binary separation. We compute the size of the mm-emission region as a function of AGN luminosity and Eddington ratio (See Appendix B) and so determine which MBHBs have mm-emission regions larger than their binary separation. We exclude these from the population estimates below.

The final criterion, that both binary components be bright, is not only a sensitivity issue (which we address in the next section) but a matter of calibration necessary for VLBI. If only one binary component is bright enough to detect, its orbital path cannot be tracked without a bright source (within $\sim 1^\circ$) for phase reference (*e.g.* Broderick *et al.* 2011), *i.e.*, the required $\sim \mu\text{as}$ astrometric precision is only possible via relative astrometry. We can make a crude estimate for the probability of finding a bright source within 1° of the target source from the number of ALMA calibrator sources. Taking that there are about 2000 adequate calibrator sources that could be used as phase references, we can estimate a lower limit on the alignment probability by assuming that these calibrators are distributed isotropically on the sky. Then the probability of finding a suitable phase reference within 1° of the source is $2000/(41252\text{deg}^2) \approx 0.05$. This is non-zero, but not large enough to be reliable. If instead the number of calibrators can be increased by a factor of 10, the probability of finding a nearby phase reference is considerable, 50%.

In the case that both binary components are bright in mm-wavelengths, the problem is eliminated as each component can phase reference its companion. Because we do not know the fraction of binaries for which both components are mm-bright, and how this depends on binary parameters, AGN type, or other unknowns, we parameterize this uncertainty with f_{**} .

3. A POPULATION OF RESOLVABLE MBHBs

3.1. Calculation

We next estimate the number of MBHBs that are emitting bright, mm-wavelength radiation due to accretion, and that have an orbital separation large enough to be resolvable by an Earth-sized VLBI array, but small enough to have a period observable in a human lifetime.

We assume that a fraction f_{bin} of mm-bright active galactic nuclei (AGN) are synonymous with accreting MBHBs. While this fraction is not robustly constrained, a number of theoretical arguments imply that its value may be of order unity (Kauffmann and Haehnelt 2000; Hopkins *et al.* 2007a). Additionally, the quasar lifetime (Martini 2004) is in agreement with the time for a binary to migrate from the edge of a gravitationally stable gas disk down to merger via gas torques and gravitational wave losses (Haiman *et al.* 2009, however, the LLAGN lifetime may be $\sim 10 - 100\times$ longer (Hopkins *et al.* 2007b)). Also, recent searches for MBHB candidates as periodically variable quasars estimate values of $f_{\text{bin}} \sim 0.3$ (D’Orazio *et al.* 2015a; Charisi *et al.* 2016) from the fraction of candidates found at a given binary period. We compute our own constraints on the binary fraction, of the population of low-luminosity AGN considered here, in §3.2 below.

We calculate the time that a MBHB with total mass M spends at a given orbital period P during the bright AGN phase. We assume that gas and gravitational radiation drive the binary to merger to compute a residence time at binary

separation a ,

$$t_{\text{res}} \equiv \frac{a}{\dot{a}} = \begin{cases} \frac{20}{256} \left(\frac{P}{2\pi}\right)^{8/3} \left(\frac{GM}{c^3}\right)^{-5/3} q_s^{-1} & P < P_{\text{trans}} \\ \frac{q_s}{4\dot{M}} t_{\text{Edd}} & P \geq P_{\text{trans}} \end{cases}$$

$$P_{\text{trans}} = 2\pi \left(\frac{16}{5}\right)^{3/8} \left(\frac{G}{c^3}\right)^{5/8} q_s^{3/4} M^{5/8} \left(\frac{\dot{M}}{t_{\text{Edd}}}\right)^{-3/8} \quad (2)$$

where the first term is the residence time due purely to gravitational wave decay (Peters 1964), and the second term is a prescription for orbital decay due to gaseous effects given by Loeb (2010). Here $q_s \equiv 4q/(1+q)^2$ is the symmetric binary mass ratio, where the standard mass ratio is given by $q \equiv M_2/M_1$; $M_2 \leq M_1$; $M_2 + M_1 = M$. The Eddington time, $t_{\text{Edd}} \equiv M/\dot{M}_{\text{Edd}} \sim 4.5 \times 10^7$ yr, is the time it takes to accrete a binary mass of material M at the Eddington accretion rate, $\dot{M}_{\text{Edd}} \equiv L_{\text{Edd}}/(\eta c^2)$, assuming an accretion efficiency of $\eta = 0.1$.

In the gas-driven case, the simple assumption is that the binary orbit shrinks via interaction with the environment, either by gas accretion, or application of positive torque to a circumbinary disk (*e.g.*, Rafikov 2016). Because this rate is uncertain (even its sign, *e.g.*, Tang *et al.* 2017; Miranda *et al.* 2017), we parameterize the gas-driven orbital decay rate in terms of an Eddington rate $\dot{M} = \dot{M}/\dot{M}_{\text{Edd}}$. The parameter \dot{M} controls the rate at which the binary orbit decays ($\dot{a} \propto \dot{M}$ in Eq. 2), not the accretion rate that determines the accretion luminosity. Hence even for the case of LLAGN, which may not experience gas inflow at the Eddington rate, we still consider mechanisms that drive the MBHB together at a rate comparable to if the binary torques were expelling gas at the Eddington rate. Essentially, due to uncertainties in binary orbital decay rates, we have purposefully not locked together the accretion mechanism and the binary decay mechanism, we have simply parameterized the decay rate in terms of an Eddington rate. The transition orbital period P_{trans} delineates gas-driven and gravitational-wave-driven orbital decay.

In the gas-driven case, the simple assumption is that the binary shrinks by applying positive torque to a circumbinary disk. Then the fraction of the inflowing gas that is expelled by the binary, and hence the binary decay rate, is parameterized in terms of the Eddington rate at which gas can be supplied to the binary $\dot{M} = \dot{M}/\dot{M}_{\text{Edd}}$. The parameter \dot{M} represents the rate at which gas is expelled by binary torques, not the accretion rate that determines the accretion luminosity. The transition orbital period P_{trans} delineates gas-driven and gravitational-wave-driven orbital decay.

From the binary residence time, we generate a probability distribution function $\mathcal{F}(M, z)$ that provides the probability that a quasar at a given redshift z , and luminosity $L = f_{\text{Edd}} L_{\text{Edd}}(M)$ harbors a MBHB with orbital period in the specified VLBI range. This probability function is derived by integrating the residence time in Eq. (2) over periods and mass ratios which meet the minimum VLBI separation requirement and the maximum period requirement, P_{base} , and normalizing by the same integral over all possible binary pa-

rameters,

$$\begin{aligned}\mathcal{F}(M, z) &= f_{\text{bin}} \frac{\int_{q_s^{\text{Vmin}}}^1 \int_{P_{\text{lo}}}^{P_{\text{hi}}} t_{\text{res}}(M, q_s, P) dP dq_s}{\int_{q_s^{\text{Pmin}}}^1 \int_0^{P_{\text{max}}} t_{\text{res}}(M, q_s, P) dP dq_s} \\ P_{\text{lo}} &= \frac{2\pi (\theta_{\text{min}} D_A(z))^{3/2}}{\sqrt{GM}} \\ P_{\text{max}} &= \frac{2\pi a_{\text{max}}^{3/2}}{\sqrt{GM}} \\ P_{\text{hi}} &= \min(P_{\text{base}}, (1+z)P_{\text{max}}).\end{aligned}\quad (3)$$

The normalization introduces three additional parameters. The first two are the minimum (symmetric) mass ratio of the entire MBHB population q_s^{Pmin} , and the minimum for the resolvable population q_s^{Vmin} . We adopt a flat distribution in mass ratio and fiducially set the two equal to 0.01, a value motivated by the minimum mass ratio for which dynamical friction can form a central binary (Callegari *et al.* 2011; Mayer 2013). We also vary q_s^{Vmin} to larger values to determine the mass ratio dependence of our results. We note that q_s^{Vmin} could have a dependence on binary mass, for example observationally through the Eddington luminosity and flux sensitivity. However, in accordance with our choice of a flat mass ratio distribution, we do not explore this possibility here.

The third new parameter is a_{max} , the maximum binary separation for which radio-loud quasar activity is triggered. This is required because the residence time due to gas accretion (large a_{max}) is independent of the binary separation (the binary spends equal time per $\ln a$ in the gas-driven phase), and hence, we cannot simply set an a_{max} in the normalization to corresponds to a quasar (or LLAGN) lifetime. As noted above however, the observationally inferred AGN lifetime is similar to that required for a MBHB to migrate through a gas disk with an outer edge set by the Toomre stability limit (Goodman 2003; Haiman *et al.* 2009), where the gas disk fragments into stars. We use this separation, corresponding to the outer edge of a gravitationally stable disk, to motivate fiducial parameter choices below.

The number of MBHBs out to redshift z , over the entire sky, with binary separation resolvable by a VLBI array, and with orbital period limited by P_{base} is,

$$\begin{aligned}N_{\text{VLBI}} &\approx 4\pi \int_0^z \frac{d^2V}{dz d\Omega} \int_{L_{\text{mm}}^{\text{min}}}^{\infty} \frac{d^2N}{dL_{\text{mm}} dV} \mathcal{F}(\chi; L_{\text{mm}}, z) dL_{\text{mm}} dz \\ \chi &= (\theta_{\text{min}}, a_{\text{max}}, \dot{M}, f_{\text{Edd}}, P_{\text{base}}, q_s^{\text{Vmin}}, f_{\text{bin}}, f_{**}),\end{aligned}\quad (4)$$

where, from left to right, we incorporate the cosmological volume element in a flat universe (*e.g.* Hogg 1999), a mm-wavelength AGN luminosity function (mmALF; see Appendix A), and the binary probability distribution function discussed above. We have re-written the binary probability in terms of mm-wavelength luminosity through the relation,

$$M = \frac{L_{\text{bol}}(L_{\text{mm}}^{\text{obs}})\sigma_T}{f_{\text{Edd}} 4\pi G m_p c} M_{\odot}, \quad (5)$$

where we have assumed that the accretion on to the binary generates bolometric luminosity equal to a fraction f_{Edd} of the Eddington Luminosity ($L_{\text{Edd}} = 4\pi G M m_p c / \sigma_T$) and we estimate the bolometric luminosity from the observed mm-wavelength luminosity (see below).

In choosing f_{Edd} , recall that LLAGN are expected to have mm-wavelength emission emanating from a small region around each BH, making them well-suited for the imaging study proposed here. To incorporate LLAGN we choose a distribution $P(x)$ of the log Eddington fraction, $x \equiv \log_{10} f_{\text{Edd}} \leq 0$, that consists of a power law with a slope $a = -0.3$ and minimum value of $x_{\text{min}} = -5.5$, plus a Gaussian in x with mean at $x_0 = -0.6$ and standard deviation $\sigma = 0.3$,

$$P(x) = \frac{(10^x)^a + \frac{1}{\sqrt{2\pi\sigma}} \exp[-(x-x_0)^2/(2\sigma^2)]}{\frac{1}{2} \left[\text{erf}\left(\frac{x_0-x_{\text{min}}}{\sqrt{2}\sigma}\right) - \text{erf}\left(\frac{x_0}{\sqrt{2}\sigma}\right) \right] + \frac{1-10^{ax_{\text{min}}}}{a \ln 10}}. \quad (6)$$

We plot $P(x)$ in Figure 1. This choice is based on observations of a normally distributed population of AGN accreting near Eddington, and a power law tail of LLAGN (Kauffmann and Heckman 2009; Shankar *et al.* 2013, but see also Weigel *et al.* (2017)). The value of x_{min} is based on Figure 5 of Eracleous *et al.* (2010). While this f_{Edd} distribution comprises our fiducial model, we also employ a simpler delta function f_{Edd} distribution for comparison.

The lower limit on the observed, specific luminosity is written in terms of the specific flux sensitivity $F_{\text{mm}}^{\text{min}}$ of the mm-VLBI instrument,

$$L_{\nu}^{\text{min}} = \frac{L_{\nu}}{L_{(1+z)\nu}} 4\pi D_L^2 \frac{F_{\nu}^{\text{min}}}{1+z}. \quad (7)$$

where the first term is the K-correction, which accounts for a luminosity difference of the quasar in the emitted $((1+z)\nu)$ and the observed (ν) bands. We use a fiducial value of $F_{\nu}^{\text{min}} = 1 \text{ mJy}$ for $\nu \sim 300 \text{ GHz}$ (mm wavelength), motivated by near-future capabilities of the Event Horizon Telescope (Broderick *et al.* 2011).

To compute the K-correction, and to construct the mm-wavelength luminosity function from a radio luminosity function, we assume that the spectral energy distribution (SED) of Radio-loud AGN is a power law, $\nu L_{\nu} \approx \nu^{0.9}$, over the frequency range $9 \lesssim \log_{10}(\nu/\text{Hz}) \lesssim 12$ (Elvis *et al.* 1994). This approximation is valid for LLAGN, as well as regular radio-loud AGN, because the radio to millimeter portion of radio-loud AGN spectra is similar for LLAGN and normal AGN (Fernández-Ontiveros *et al.* 2012).

To scale from L_{mm} to a bolometric luminosity for LLAGN we use a median bolometric correction from 2 – 10 keV of 50 (Eracleous *et al.* 2010). Because νL_{ν} in the millimeter is within a factor of a few of νL_{ν} in the 2 – 10 keV range (Fernández-Ontiveros *et al.* 2012), and because there is a large scatter in the value of the bolometric correction in the X-ray range, we adopt $L_{\text{bol}} = 50 \nu_{\text{mm}} L_{\text{mm}}$.

By calculating N_{VLBI} in this way, the mass distribution of binaries is provided through the AGN luminosity function. We stress again that the parameter f_{Edd} , along with the accretion efficiency $\eta = 0.1$ relates the accretion rate on to the binary to the observed bolometric luminosity. This is independent of \dot{M} above which parameterizes the binary decay rate.

For each computation of the integrand in Eq. (4), corresponding to a value of the bolometric luminosity, we draw a value of $\log_{10} f_{\text{Edd}}$ from the chosen Eddington fraction distribution. The value of $\log_{10} f_{\text{Edd}}$ is used to convert the luminosity for which the mmALF is evaluated to a binary mass for which the probability \mathcal{F} is evaluated. The probability also

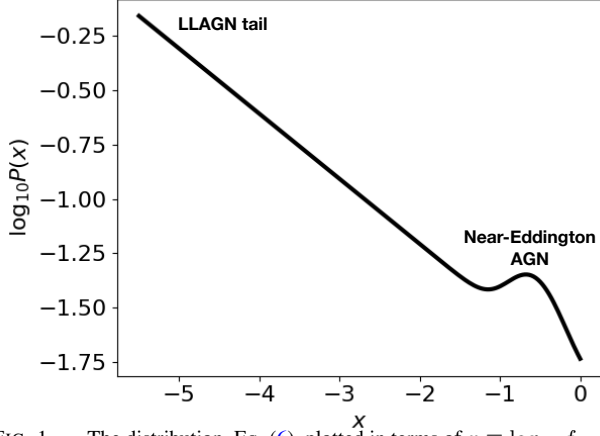


FIG. 1.— The distribution, Eq. (6), plotted in terms of $x \equiv \log_{10} f_{\text{Edd}}$.

depends on the size of the mm-wavelength emission region. This is calculated from the luminosity and compared to the size of the binary separation which depends on the binary mass through the value of the Eddington ratio (Appendix B).

One caveat of our implementation is that the Eddington fraction distribution is constructed as to match observations of low-luminosity, nearby AGN, and not necessarily radio-loud AGN (*i.e.*, we have assumed that the f_{Edd} distribution is the same for both radio-loud and radio-quiet populations.). Meanwhile the mmALF we use is aimed at large redshifts for only radio-loud AGN. The use of one with the other can cause extrapolation to very large BH masses. This is because, at large z , only the most luminous AGN can be observed. For a given Eddington fraction distribution, the most luminous AGN must be powered by the most massive MBHs. Because the LLAGN Eddington distribution samples very low values, the mapping from luminosity to binary mass can result in very large values of the MBH mass, above $10^{10} M_{\odot}$. It is likely that such MBHs do not exist, but rather, that there would be a preference for the Eddington distribution to sample larger values of f_{Edd} at higher redshifts. To get around this artificial MBH mass inflation, we simply make a cut in the mass distribution, so that, effectively, low values of f_{Edd} are not sampled at high

luminosities and high redshifts. Essentially we are requiring that the LLAGN Eddington distribution we have employed is correct for low redshifts where it is derived, but then to extrapolate to high redshifts, we enforce that the resulting MBH masses are consistent with observed maximum masses. We implement this by multiplying the binary probability \mathcal{F} by a factor $\exp[-(M/M_{\text{max}})^4]$. As a fiducial value we choose $M_{\text{max}} \sim 10^{10} M_{\odot}$.

Choosing a maximum binary orbital period of $P_{\text{base}} = 10$ years and choosing a minimum binary mass ratio of the entire MBHB population of $q_s^{\text{Pmin}} = 0.01$, we are left with the free parameters θ_{min} , f_{**} , f_{bin} , q_s^{Vmin} , a_{max} , and $\dot{\mathcal{M}}$. For mm VLBI, θ_{min} is dominated primarily by uncompensated propagation delays caused by the troposphere, rather than contributions due to thermal noise that scale with the inverse of the signal-to-noise ratio (Reid and Honma 2014; Broderick *et al.* 2011). Hence we do not adopt a signal-to-noise ratio-dependent resolution. Instead, we treat θ_{min} as a parameter that elucidates the gain in resolvable MBHBs that can be achieved with better resolution limits. As motivated by the gravitational wave background upper limits in the next section, we set $f_{\text{bin}} = 0.05$. We set $f_{**} = 1$ throughout, as the result scales linearly with this factor. Then we determine the dependence of N_{VLBI} on the turn-on separation a_{max} , minimum (symmetric) mass ratio of the resolvable population q_s^{Vmin} , and gas driven migration rate $\dot{\mathcal{M}}$ out to a given redshift. The parameters of our model and their fiducial values are given in Table 1 for reference.

3.2. Gravitational Wave Background

Before examining the population of resolvable MBHBs, we use the results of the previous section to compute the contribution to the stochastic gravitational wave background (GWB) of all MBHBs in this mock population and enforce consistency with current limits from the PTAs.

The frequency dependent, characteristic strain due to the gravitational wave background is (Phinney 2001),

$$h_c^2(f) = \frac{G}{c^2} \frac{4}{\pi f_r^2} \int_0^\infty \int_0^\infty \int_{q_s^{\text{Pmin}}}^1 \frac{d^3 n}{dz dM dq} \frac{1}{1+z} \frac{dE_{\text{GW}}}{d \ln f_r} dq dM dz. \quad (8)$$

Here f_r is the rest frame frequency of the GWs. Assuming circular binaries, f_r is equal to twice the Keplerian orbital period of the binary. The first term under the integrand is the co-moving number density of inspiraling MBHBs per redshift z , binary mass M , and mass ratio q . Continuing the assumption of circular binary orbits, each MBHB emits GW energy per log frequency (Sesana *et al.* 2008),

$$\frac{dE_{\text{GW}}}{d \ln f_r} = \frac{dt_r}{d \ln f_r} \frac{32}{5} \frac{G^{7/3}}{c^5} (\pi M_c f_r)^{10/3} = \frac{64}{15} \frac{G^{7/3}}{c^5} (\pi M_c f_r)^{10/3} t_{\text{res}}, \quad (9)$$

where we have rewritten the rest frame time per log frequency in terms of the residence time of the binary at a given separation (see, *e.g.*, Kocsis and Sesana 2011). This residence time is given by Eq. (2) for $a \leq a_{\text{max}}$ and by the gravitational wave residence time for $a > a_{\text{max}}$. Here $M_c(M, q) \equiv M q^{3/5} / (1+q)^{6/5}$ is the chirp mass of the binary and q is related to the symmetric mass ratio via the expression in the discussion below Eq. (2).

For the co-moving number density we use the luminosity function from the previous section (see Appendix A), mapping luminosity to binary mass via Eq. (5). We further assume a flat distribution of mass ratios from q_s^{Pmin} to 1. Then the GWB strain becomes,

$$h_c^2(f) = \frac{G^{10/3}}{c^7} \frac{256}{15 \pi f_r^2} \int_0^\infty \int_0^\infty \frac{d^2 n}{dz dM} \left\langle (\pi M_c f_r)^{10/3} \frac{t_{\text{res}}}{(1+z)} \right\rangle_{q_s} dz dM, \quad (10)$$

Parameter	Meaning	Fiducial Value	LLAGN Value	Notes
Decay Model				
\mathcal{M}	Gas supply rate in units of Eddington	1.0	"	Fraction of supply rate controlling migration rate, not luminosity
a_{\max}	Separation where binary becomes active	0.1 pc	"	Needed because residence time in gas dominated regime is independent of a
q_s^{Vmin}	Minimum binary symmetric mass ratio in VLBI sample	0.01	"	—
q_s^{Pmin}	Minimum binary symmetric mass ratio of all MBHBs	0.01	"	—
— — Additional decay-model parameters that are not varied — —				
f_{Edd}	Fraction of Eddington luminosity	$10^{-4.1}$	Eq. (6)	Relates M to L_{bol}
η	Accretion efficiency	0.1	"	—
f_{bin}	Fraction of AGN triggered by MBHBs	0.05	"	—
M_{\max}	Maximum allowed MBHB mass	$10^{10} M_{\odot}$	"	See the end of §3.1
$L_{\text{bol}}/L_{\text{mm}}$	Bolometric correction from millimeter	50	"	Estimate based on Eracleous et al. (2010)
Observational				
θ_{\min}	Minimum angular resolution	$1 \rightarrow 30 \mu\text{s}$	"	Broderick et al. (2011)
F_{\min}	mm-Flux sensitivity	1 mJy	"	Broderick et al. (2011)
P_{base}	Maximum observed binary period	10 years	"	Detectable in human lifetime
f_{**}	Fraction of MBHBs with <i>both</i> BHs mm-bright	1.0	"	—

TABLE 1
PARAMETERS OF THE MODEL AND THEIR FIDUCIAL VALUES UNLESS STATED OTHERWISE.

where $\langle \cdot \rangle_{q_s}$ denotes an average over the symmetric mass ratio, q_s .

The GWB characteristic strain associated with the radio-loud MBHBs is plotted versus GW frequency in Figure 2 for four different sets of parameters dictating the gas-driven decay, and assuming the power law plus Gaussian Eddington ratio distribution described in the previous section. The dashed-gray line plots the approximate, current PTA upper limits assuming GW decay alone and scaled to the currently most stringent PTA upper limits at a single frequency ([Sesana et al. 2017](#); [Shannon et al. 2015](#)). The hatched orange region represents the approximate range of GW frequencies for which mm-VLBI-resolvable MBHBs will reside, while the gray shaded region represents the approximate PTA frequency range.

For the fiducial parameters (solid-orange line), the GWB is dominated by gravitational decay as can be seen by the $f_{\text{GW}}^{-2/3}$ decline in the background at low frequencies. The increase in slope above $\sim 10^{-7}\text{Hz}$ is due to the removal of MBHBs that would be at separations smaller than that of the last stable orbit corresponding to the binary mass ($a = 6GM/c^2$).

Increasing both $\dot{\mathcal{M}}$ and a_{\max} increases the impact of the gas-driven decay on the GWB at low frequencies, in agreement with the studies of [Kelley et al. \(2017a\)](#) and [Kocsis and Sesana \(2011\)](#). This can be seen by the turn over of the green dashed and pink dot-dashed lines in Figure 2 at low frequencies. The gas moves the binary through this larger separation regime more quickly than GW-driven decay alone.

We find that the population of radio-loud AGN must have a MBHB fraction of $\lesssim 0.05$ for consistency of our model with the upper limits on the PTA GWB. Hence we use that $f_{\text{bin}} = 0.05$ as our fiducial MBHB fraction throughout.

We note that there are many studies of the GWB from model MBHB populations that find agreement with the PTA upper limits, but with a less stringent constraint on the fraction of MBHB harboring AGN (see [Kocsis and Sesana 2011](#); [Kelley et al. 2017b,a](#); [Mingarelli et al. 2017](#), and references therein). The stringency of the limit derived here is the inclusion of LLAGN via the Eddington distribution plotted in Figure 2; the many AGN at low Eddington ratios implies more

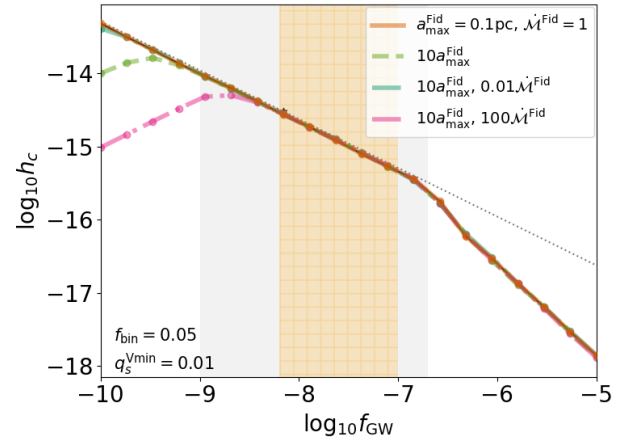


FIG. 2.— The gravitational wave background of radio-loud MBHBs, assuming that 5% of radio-loud AGN harbor a MBHB. The dashed gray line is the GW background due to gravitational wave-driven decay alone and with amplitude calibrated by PTA upper limits. The gray shaded region is the approximate PTA frequency range, and the hashed orange region is the range of inspiral frequencies where MBHBs could be resolvable by millimeter VLBI.

MBHBs at higher masses. This is evidenced in the non-trivial dependence of the GWB on the choice of Eddington fraction distribution. If, for example, we choose $x_{\min} = -4$ instead of the fiducial $x_{\min} = -5.5$ in Eq. (6), then the inferred GWB strain is an order of magnitude smaller, and hence f_{bin} is not constrained at all. We further note that this GWB is calculated using the radio-loud luminosity function, which accounts for 10% of the AGN. However, as discussed above, our value of $f = 0.05$ is already quite conservative and dependent on the Eddington distribution fraction. Hence, we simply take a fiducial value of $f = 0.05$ which is the minimal constraint taking into account all of the MBHBs represented in our model and move forward within our toy-model, using the already motivated choice of Eddington fraction distribution. We leave exploration of this distribution, and consequences for the GWB, to future work.

4. RESULTS

4.1. Number of resolvable MBHBs: redshift distribution and dependence on angular resolution

We begin by presenting the total number of resolvable MBHBs for which an entire orbit can be tracked with VLBI. Figure 3 explores the dependence of the total number of resolvable binaries on maximum redshift and minimum instrument angular resolution. The binary fraction in AGN is assumed to be $f_{\text{bin}} = 0.05$, as constrained in §3.2. The left column varies the minimum binary mass ratio from $q_s^{\text{Vmin}} = 0.1$ to $q_s^{\text{Vmin}} = 0.9$ for $F_{\text{min}} = 1\text{mJy}$. The top two panels in the right column consider a lower and higher minimum flux sensitivity, at a fixed minimum mass ratio of $q_s^{\text{Vmin}} = 0.01$. The bottom right panel considers a larger maximum binary period at the optimal minimum mass ratio and flux sensitivity.

In the fiducial case (top left panel), which assumes no mass ratio preference for the resolvable binaries ($q_s^{\text{Vmin}} = 0.01$) and a flux sensitivity of $F_{\text{min}} = 1\text{mJy}$, we could resolve binaries with angular separations as large as $\sim 25\mu\text{as}$. This is within the diffraction limit of present day mm-VLBI. At a best case angular resolution of $\theta_{\text{min}} = 1\mu\text{as}$, a few tens of MBHBs would be resolvable with mm-VLBI. These resolvable MBHBs lie between redshift 0.05 and 0.5.

The left column of Figure 3 shows that in order to resolve at least one MBHB, one must have $q_s^{\text{Vmin}} \lesssim 0.9$, at the best case angular resolution and fiducial flux sensitivity. This implies that a resolvable population, for the fiducial binary-decay model, can not consist of preferentially equal mass binaries (but it can contain equal mass binaries).

The top right panel of Figure 3 shows that an order of magnitude improvement in flux sensitivity provides an order of magnitude increase in N_{VLBI} . This improvement in sensitivity also increases the redshift range out to $z \sim 1.0$. The improved sensitivity does not increase the range of θ_{min} at which resolvable MBHBs can be found. The middle right panel of Figure 3 shows that an order of magnitude worse flux sensitivity provides an order of magnitude decrease in N_{VLBI} . The middle right panel also shows that for $N_{\text{VLBI}} \gtrsim 1$, one must have $F_{\text{min}} \lesssim 10\text{mJy}$ for the best case q_s^{Vmin} .

Finally, the bottom right panel of Figure 3 considers a best case scenario: including MBHBs with orbital periods up to 20 years, an optimal flux sensitivity of $F_{\text{min}} = 0.1\text{mJy}$, and otherwise fiducial model parameters. We see that the number of resolvable MBHBs can be increased to a few thousand at the best case angular resolution. Including longer period binaries also yields a population of large angular separation, $\gtrsim 30\mu\text{as}$ separation binaries.

4.2. Visualization of result

We now investigate the dependence of our results presented in Figure 3 upon the parameters of our model. This allows us to determine the demographic of MBHBs that can be tracked with VLBI, and it also allows us to determine the range of results that our model could produce.

We begin by visualizing the MBHB demographics that contribute to the integral in Eq. (4). Each panel of Figure 4 plots contours of the integrand of Eq. (4) as a function of maximum binary orbital period and observed mm-wavelength flux. We scale the integrand by $4\pi z L_{\text{mm}}$, taking a representative value of $L_{\text{mm}}^* = 10^{44}/\nu_{\text{mm}} \sim 3 \times 10^{32} \text{erg s}^{-1} \text{Hz}^{-1}$ to correspond roughly to the cumulative value of the integral at that point. Contours of this scaling of the integrand of Eq. (4) are colored chartreuse to purple, denoting many MBHBs and zero MBHBs respectively. On top of the chartreuse-purple con-

tours we shade regions with different colors corresponding to the regions where our criteria for a resolvable orbit break down. That is, the overplotted-shaded regions delineate the space of resolvable (unshaded) and non-resolvable (shaded) binaries. The left-middle panel labels these regions. The resulting, trapezoid-shaped window at the center of each panel, which contains only the chartreuse-purple contours, frames the parameter space of MBHBs that are resolvable and have orbits that can be tracked in a human lifetime.

On the top horizontal axis of each panel in Figure 4, we relate the observed flux (bottom axis) to the binary total mass via the Eddington ratio. The left column of Figure 4 assumes a delta function value of the Eddington ratio, $f_{\text{Edd}} = 10^{-4.1}$, that corresponds to the expectation value of the distribution of Eq. (6). The right column samples from the full Eddington ratio distribution. Because the latter case requires a random draw of the Eddington ratio for each point in period-flux space, we generate 200 realizations and plot the average. In the right panels we also plot the average binary mass that corresponds to the flux on the lower horizontal axis (using the same 200 f_{Edd} draws). In each panel we record the fixed parameters in the bottom left.

The darkest regions to the left of the thick black lines represent binaries that are dimmer than the limiting flux $F_{\text{mm}}^{\text{min}}$. For the fixed $f_{\text{Edd}} = 10^{-4.1}$ Eddington ratio case (left column of Figure 4), at $z = 0.1$, MBHBs with total mass $\gtrsim 10^{8.5} M_{\odot}$ are detectable at a limiting flux of $F_{\text{mm}}^{\text{min}} = 1\text{mJy}$. By $z = 0.5$, there are no more MBHBs below $\sim 10^{10} M_{\odot}$ that are detectable above 1mJy .

In the right column, this darker-shaded region corresponds to the same flux limit as the left column, but this corresponds to a different binary mass via the Eddington ratio distribution in Eq. (6). In this case, using the power law plus Gaussian distribution, the same fluxes correspond to higher mass binaries. At $z = 0.1$, MBHBs with total mass of $\gtrsim 10^9 M_{\odot}$, on average, are detectable at a limiting flux of $F_{\text{mm}}^{\text{min}} = 1\text{mJy}$. By $z = 0.5$, only rare MBHBs with mass $\gtrsim 10^{10.5} M_{\odot}$ can be bright enough to exceed the flux limit. Hence, binaries can be resolved out to $z \sim 0.5$, limited by the minimum detectable mm-wavelength flux. These binaries will preferentially be more massive at higher redshifts.

Note that in the right columns, contours for the scaled integrand of Eq. (4) do not plunge abruptly at the maximum cut-off mass as they do in the left panels. This is due to the averaging of M for many draws of f_{Edd} .

The red regions, lying outside of the thick red trapezoid, represent the space of restricted binary orbital parameters. Below the bottom-left red line, for smaller masses and periods, the binary is too compact to be resolvable at the quoted redshift and minimum instrument angular resolution (this being the P_{min} limit of integration in Eq. (4)). The bottom-right red line is the orbital period at $a = 6GM/c^2$, which we label ISCO. The top, horizontal red line is the imposed maximum observed orbital period (P_{base}). To the far top right, the small restricted region at the longest periods and largest binary masses is where the period at turn-on separation a_{max} is shorter than the maximum baseline period (see definition of P_{hi} in Eq. 4).

In both left and right columns, it is evident that the trapezoid-shaped window defined by the red regions gets smaller and moves to lower fluxes at higher redshifts. Both behaviors are a combination of three effects: i) the minimum angular resolution corresponds to a larger physical binary sep-

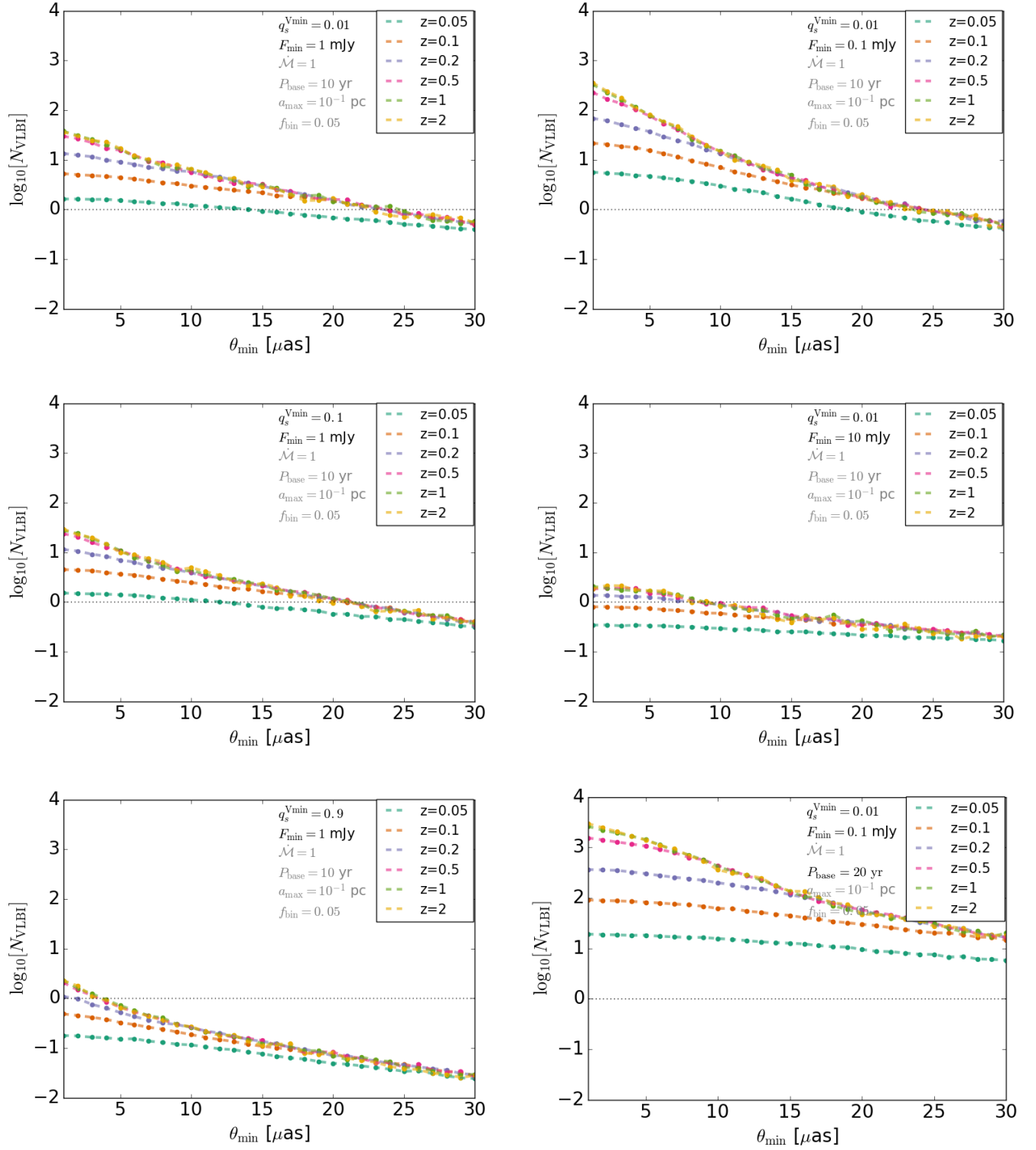


FIG. 3.— The number of resolvable MBHBs over the entire sky as a function of minimum instrument angular resolution θ_{min} for different maximum redshifts (labeled). The left column fixes the flux sensitivity to the fiducial value but increases the minimum binary mass ratio. The top right panel enhances the instrument flux sensitivity, the middle right panel worsens the instrument flux sensitivity, and the bottom right panel shows the gain due to increasing the maximum baseline period at the best case flux sensitivity.

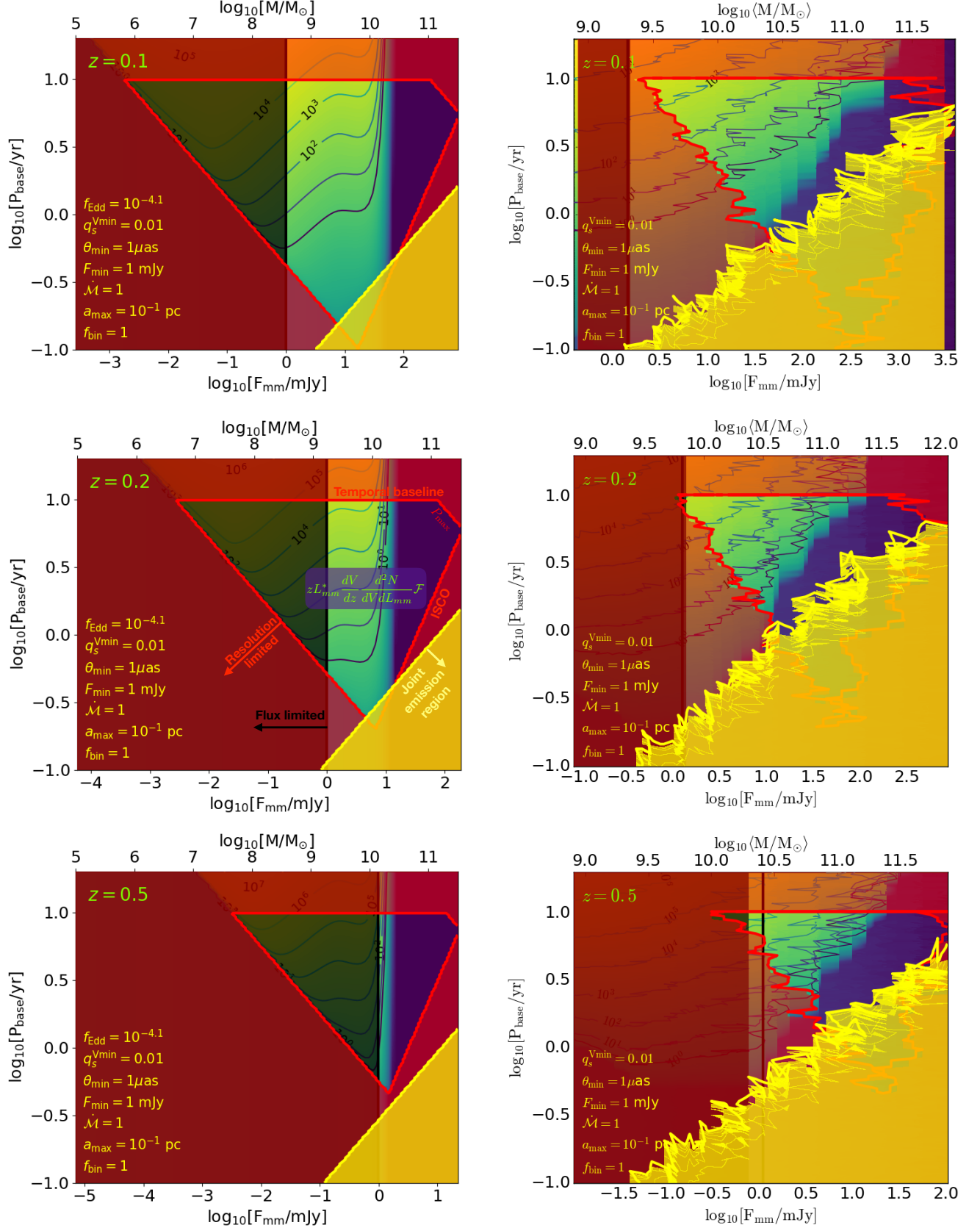


FIG. 4.— Visualization of the integral of Eq. (4). The left middle panel is labeled as a guide to the the different regions plotted in each panel. The left column assumes a delta function value of the Eddington ratio, $f_{\text{Edd}} = 10^{-4.1}$. The right column assumes a power law plus Gaussian distribution of f_{Edd} (Eq. 6) and averages over 200 f_{Edd} draws. From top to bottom, each row is for redshift $z = 0.1, 0.2$, and 0.5 . The labeled contours, shaded from chartreuse to purple, are a scaling of the integrand in Eq. (4), with chartreuse indicating many MBHBs and purple indicating none. The differently colored shaded regions, overplotted on these contours, denote where our criteria for a MBHB to be a VLBI tracking target are not met. Hence, the trapezoid-shaped window in the center of each panel delineates the region of parameter space where MBHBs can be resolved and tracked along their orbits with VLBI. The **darker-shaded regions**, bounded on the right by the thick black line, are where emission is too dim to detect, given the labeled minimum flux sensitivity. The **red-shaded regions**, external to the thick red lines, are where the binary is not resolvable either because it is below the minimum resolvable separation, above the maximum baseline orbital period, or at merger. The **yellow-shaded regions** are where the mm-emission region is larger than the binary separation.

aration at greater distances, ² ii) higher flux systems do not exist at larger distances because of the limiting intrinsic luminosity set by the maximum binary mass and the Eddington ratio distribution, and iii) at larger distances, higher flux systems correspond to more massive binaries; for a fixed binary period these systems have smaller binary separations and are less likely to lie above the limiting angular resolution.

The yellow region, in the bottom right of each panel, represents where the mm-wavelength emission region is larger than the binary separation. This occurs for the closest separation (shortest orbital period) and brightest systems because brighter emission corresponds to a larger photosphere (see Appendix B). For the low Eddington ratios chosen here, only the more rare, short period, high mass binaries are obscured by a large photosphere. This is of course the reason that we consider LLAGN for this study. Figure 7 shows that for Eddington ratios larger than ~ 0.1 (and even lower for worse angular resolution limits) obscuration by a large mm-photosphere engulfs what would otherwise be a resolvable binary.

Summarizing Figure 4, we find that:

- The number of resolvable MBHBs becomes flux limited at $z \gtrsim 0.5$ (for $F_{mm}^{\min} = 1\text{mJy}$).
- MBHBs with total mass of $10^7 - 10^8 M_\odot$ and with the longest orbital periods contribute the most to N_{VLBI} . However, the relevant flux sensitivity results in a preference for the brightest, highest mass systems. Increasing P_{base} always yields more resolvable MBHBs.
- The most massive and shortest period binaries are obscured by a large mm-wavelength emission region.
- Lower mass and shorter period binaries are excluded by angular resolution requirements.
- For the small Eddington ratios considered here, the mm-emission region size constraints do not exclude much of the parameter space. Size constraints do become important, however, for Eddington ratios closer to unity (see Figure 7 below).

4.3. Parameter dependencies

Now that we have explored the make up of MBHBs that contribute to the integral in Eq. (4), we explore the dependence of the result, N_{VLBI} , on the major model parameters. The most important parameters controlling the binary decay model are the turn-on separation a_{max} , the minimum binary mass ratio q_s^{Vmin} and the gas driven decay rate \dot{M} . In Figure 5 we explore the dependence of N_{VLBI} on these parameters for three values of the minimum angular resolution. On the left vertical-axis of each panel we plot the angular scale corresponding to a_{max} at $z = 0.2$. In each panel, we record the fixed parameters in the top left. We graphically mark the fiducial values of the parameters being varied by green lines intersecting at a green point. The white lines are contours of constant residence time in units of years. These are drawn for a representative binary with $M = 10^9 M_\odot$ and $q_s = 0.1$ (left column) or $M = 10^9 M_\odot$ and $\dot{M} = 1$ (right column) and labeled in units of years.

² This is the case at the redshifts of interest here. For $z \gtrsim 1.6$, this relation reverses due to cosmology.

To demonstrate the full parameter dependencies of N_{VLBI} , we draw contours of N_{VLBI} in Figure 5 assuming a value of $f_{\text{bin}} = 1$. Note, however, that the gravitational wave analysis of the previous section requires $f_{\text{bin}} \lesssim 0.05$. Hence, Figure 5 shows that, for minimum resolutions ranging from 1 to $20\mu\text{as}$, the binary decay model predicts a total of $N_{\text{VLBI}} \sim f_{**} f_{\text{bin}} 10^3$ resolvable binaries at the fiducial parameter values of $F_{mm}^{\min} = 1\text{mJy}$, $a_{\text{max}} \sim 0.1\text{ pc}$, $q_s^{\text{Vmin}} = 0.01$, and $\dot{M} \sim 1.0$. For the range of plausible parameter space, and relaxing the GWB limit, this number can range up to $\sim 10^5$. Next we discuss the dependence of N_{VLBI} on these parameter values.

- **a_{max} dependence:** Above and below $a_{\text{max}} \sim 10^{-1.75}\text{ pc}$, N_{VLBI} decreases. For $a_{\text{max}} \gtrsim 10^{-1.75}\text{ pc}$ this results from the assumption that a_{max} corresponds to where the binary becomes bright and, simultaneously, where gas-driven orbital decay begins. For larger values of a_{max} , the range of binary separations over which the binary is bright becomes larger while the range of binary separations over which it is resolvable stays the same. Put another way, for larger a_{max} , the space of possible binary parameters for which the binary is bright increases in size while the target range does not, and so the probability that any bright MBHB system is in the resolvable range decreases.

For $a_{\text{max}} \lesssim 10^{-1.75}\text{ pc}$, the space of possible binary parameters over which the binary is resolvable decreases because the binaries with the longest allowed periods ($P \rightarrow P_{\text{base}}(1+z)$) have separations larger than a_{max} and hence are not bright all of their resolvable lifetime. N_{VLBI} drops to zero at the value of a_{max} that falls below the minimum resolvable angular resolution at a given redshift. This can be seen by comparing the location of the small- a_{max} cutoff of N_{VLBI} between the $\theta_{\text{min}} = 1, 10$, and $20\mu\text{as}$ panels in Figure 5.

Physically motivated values of a_{max} are suggested by the red shaded regions in Figure 5. This region is the range of (binary mass dependent) outer radii of a gravitationally stable gas disk (Goodman 2003; Haيمان *et al.* 2009). To illustrate this range we choose a binary mass of $10^9 M_\odot$ (motivated by Figure 6 below) and compute the range of gravitationally stable outer disk radii assuming electron scattering and free-free absorption dominated opacity.

However, because the bright lifetime of an AGN is not necessarily determined by the size of a Toomre-stable disk, we leave a_{max} as a free parameter. We choose a fiducial value of $a_{\text{max}} = 0.1\text{ pc}$ to be consistent with these gravitationally stable disks, but also to correspond to a value near the peak of the N_{VLBI} distribution. It is encouraging that the most optimistic predictions for N_{VLBI} lie within this region. We do not choose a smaller a_{max} , because of possible tension with the sub-pc separations of known MBHB candidates (*e.g.* Graham *et al.* 2015b; Charisi *et al.* 2016). Smaller a_{max} , and hence larger inferred values of N_{VLBI} , are of course not ruled out.

- **q_s^{Vmin} dependence:** In the left column of Figure 5, we plot contours of N_{VLBI} in a_{max} vs. q_s^{Vmin} space. That is, we assume a minimum mass ratio $q_s^{\text{Pmin}} = 0.01$ of

the population of all MBHBs and vary the minimum mass ratio of resolvable MBHBs, q_s^{Vmin} . The utility of the q_s^{Vmin} parameter is to elucidate which mass ratios are contributing to the resolvable population. It is also useful if we wish to restrict the population of resolvable MBHBs to be only those with near unity mass ratios, to increase the probability that both will be bright. The left panels of Figure 5 clearly show that the value of N_{VLBI} only begins to strongly depend on q_s^{Vmin} when the latter approaches unity, at which point N_{VLBI} drops to zero (at $q_s \sim 0.7$ or $q \sim 0.3$). This is simply a result of positing a flat distribution of binary mass ratios.

- **$\dot{\mathcal{M}}$ dependence:** In the right column of Figure 5 we plot contours of N_{VLBI} in a_{max} vs. $\dot{\mathcal{M}}$ space. To understand the dependence of N_{VLBI} on $\dot{\mathcal{M}}$, we first consider the purely *gas-driven* scenario. In this case, N_{VLBI} does *not* depend on $\dot{\mathcal{M}}$, rather it sets the average active lifetime of the MBHB indicated by the white contours in Figure 5. The steep turn-around in these white contours is where the binary changes from gas-driven to GW-driven orbital decay. In the gas-driven regime, there is a decrease in MBHB lifetime with increasing $\dot{\mathcal{M}}$ as expected, but this is not reflected in the contours of N_{VLBI} because the binary decreases its time spent in the resolvable regime proportionally to its total lifetime. This is essentially a result of the duty-cycle argument that we use in this computation, *i.e.*, our assertion that a fraction f_{bin} of AGN are MBHBs. Reassuringly, our total MBHB lifetimes are consistent or slightly lower than observationally constrained AGN lifetime (Martini 2004). We note, however, that the bright lifetime of an LLAGN may be longer ($\sim 10 - 100\times$) than the bright Eddington-limited quasar lifetime (Hopkins et al. 2007b). Hence, choices of $\dot{\mathcal{M}}$ (and a_{max}) that lead to $\sim \text{Gyr}$ bright binary residence times may be relevant for the LLAGN.

When including GW emission, N_{VLBI} does depend on $\dot{\mathcal{M}}$ because it sets the binary separation where GW-driven decay takes over. The consequence being that larger values of $\dot{\mathcal{M}}$ correspond to binaries that spend relatively more time in the gas driven regime than in the more short-lived GW-driven regime. This affects the value of N_{VLBI} if the transition separation a_{trans} falls within a_{max} . The wider the range of separations that the binary spends in the gas driven stage, and above the minimum separation $a_{\text{min}} = \theta_{\text{min}} D_A(z)$, the more resolvable binaries we expect to find.

This explains why N_{VLBI} is constant below values of a_{max} on a line parallel to the line connecting the elbows of the white contours, the transition from gas to GW driven decay. Below this line $a_{\text{max}} < a_{\text{trans}}$, and the binary is already in the GW-driven regime when it enters the disk and becomes bright, so gas does not affect the decay. That N_{VLBI} obtains an $\dot{\mathcal{M}}$ dependence approximately above the line connecting the elbows of the white, $M = 10^9 M_\odot$ contours, means that these most-massive MBHBs dominate the resolvable population. We show that this is indeed the case in Figure 6.

The increasing dependence of N_{VLBI} on $\dot{\mathcal{M}}$ with larger

$\dot{\mathcal{M}}$ stems from the fact that larger $\dot{\mathcal{M}}$ implies a smaller a_{trans} and hence causes the binary to spend more of its resolvable lifetime in the gas dominated stage. A similar increasing importance of gas effects for larger a_{max} and smaller a_{trans} (larger $\dot{\mathcal{M}}$), can also be seen in the different GWB realizations of Figure 2.

- **Maximum period and mass dependence:** Figure 6 illustrates the demographics of resolvable MBHBs by plotting contours of N_{VLBI} as a function of an imposed maximum observed binary orbital period and a maximum binary mass. From top panel to bottom panel, the minimum angular resolution is varied from $\theta_{\text{min}} = 1$ to 10 to $20 \mu\text{as}$. The white lines show contours of constant binary separation, and the cyan lines are contours of constant gravitational wave strain at a representative redshift of $z = 0.2$. The most massive and lowest period resolvable binaries are approaching those that could be resolvable as individual GW sources. We comment on this possibility in §5.5. As expected, and pointed out in the discussion surrounding Figure 4, Figure 6 illustrates that a smaller minimum spatial resolution implies a population of resolvable binaries with periods and masses that extend to lower values.

The smallest binary masses at a maximum orbital period of ~ 10 years are $3 \times 10^6 M_\odot$ for $\theta_{\text{min}} = 1 \mu\text{as}$, $\sim 3 \times 10^7 M_\odot$ for $\theta_{\text{min}} = 10 \mu\text{as}$, and $\sim 10^8 M_\odot$ for $\theta_{\text{min}} = 20 \mu\text{as}$. The minimum observed binary periods for the largest, $10^{10} M_\odot$, MBHBs are ~ 1.5 years for $\theta_{\text{min}} = 1 \mu\text{as}$, ~ 3 years for $\theta_{\text{min}} = 10 \mu\text{as}$, and ~ 5 years for $\theta_{\text{min}} = 20 \mu\text{as}$.

5. DISCUSSION

5.1. MBHB population

VLBI imaging of a MBHB over the course of an orbit could provide the first definitive proof of a MBHB at sub-pc separations. It will also probe a regime of MBHB evolution inaccessible to GW observations. Sub-pc separations represent the poorly understood stage in MBHB evolution where GW radiation plus environmental effects are competing for dominance in binary orbital decay, but where GW emission is not yet loud enough to identify the system as an individually resolved GW source with observatories such as the PTAs or LISA (Amaro-Seoane et al. 2017). Hence, not only is this regime one of the most important to understand for deciphering, *e.g.*, the final-parsec problem, but it is also directly accessible only in the EM sector.

VLBI imaging could attain the definitive detection of multiple MBHBs, but importantly, work as a verification tool for more indirect methods of MBHB identification. Linking indirect MBHB signatures, such as quasar periodicity, variable broad lines, or jet morphology with a secure detection of a MBHB via imaging would aid in the confident use of these indirect, but more easily employed identification methods. Identification of at least a few MBHB systems with VLBI imaging could even aid in identifying yet undiscovered signatures of MBHBs in galactic nuclei.

If a population of MBHBs can be identified, the work presented in §4.3 can be inverted to infer the binary residence times given the observed number of MBHBs at given separations and redshifts. In essence, a plot similar to Figure 3 could be made from observations. From this, models for the residence times can be ruled out, and the parameters within these

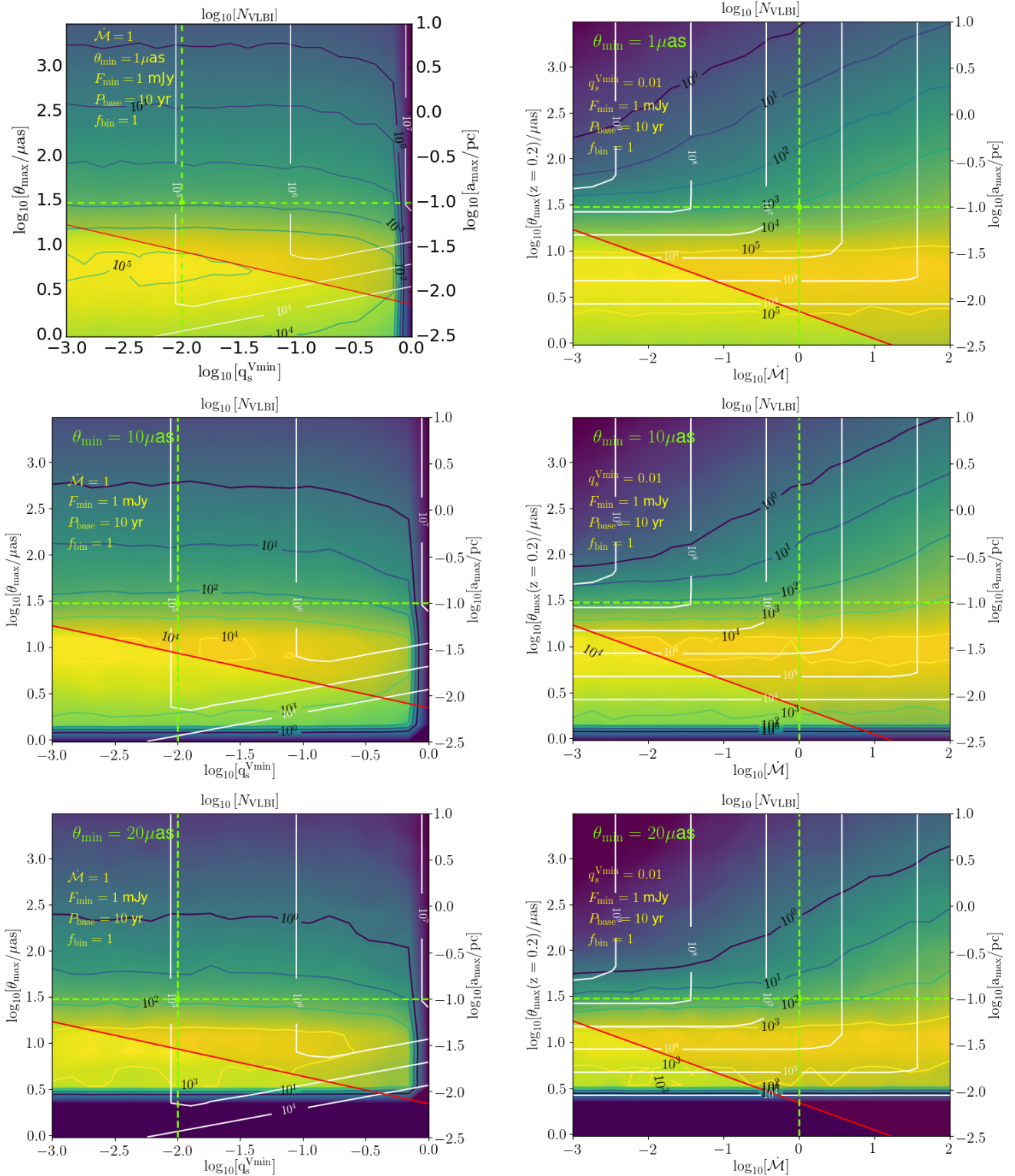


FIG. 5.— Yellow-purple shaded contours represent the Log number of resolvable MBHBs over the entire sky, as a function of the main model parameters, namely: a_{\max} , setting the orbital separation at which the binary enters a gas disk and becomes a radio-loud AGN; $q_s^{V\min}$, the minimum binary symmetric mass ratio of the resolvable population (left column); and \mathcal{M} , which determines the gas-driven orbital decay rate (right column). The labeled white lines are contours of constant residence time, in years for a $10^9 M_{\odot}$ MBHB with $q_s^{V\min} = 0.1$ (left column) and $\mathcal{M} = 1$ (right column). From top to bottom, we consider minimum instrument resolutions of $\theta_{\min} = 1, 10$, and $20 \mu\text{as}$. The dashed-green lines mark the chosen fiducial parameter values. In all panels the red-shaded region indicates the possible (binary mass dependent) locations of the outer edge of a Toomre-stable, steady-state accretion disk, which may be important for determining the value of a_{\max} .

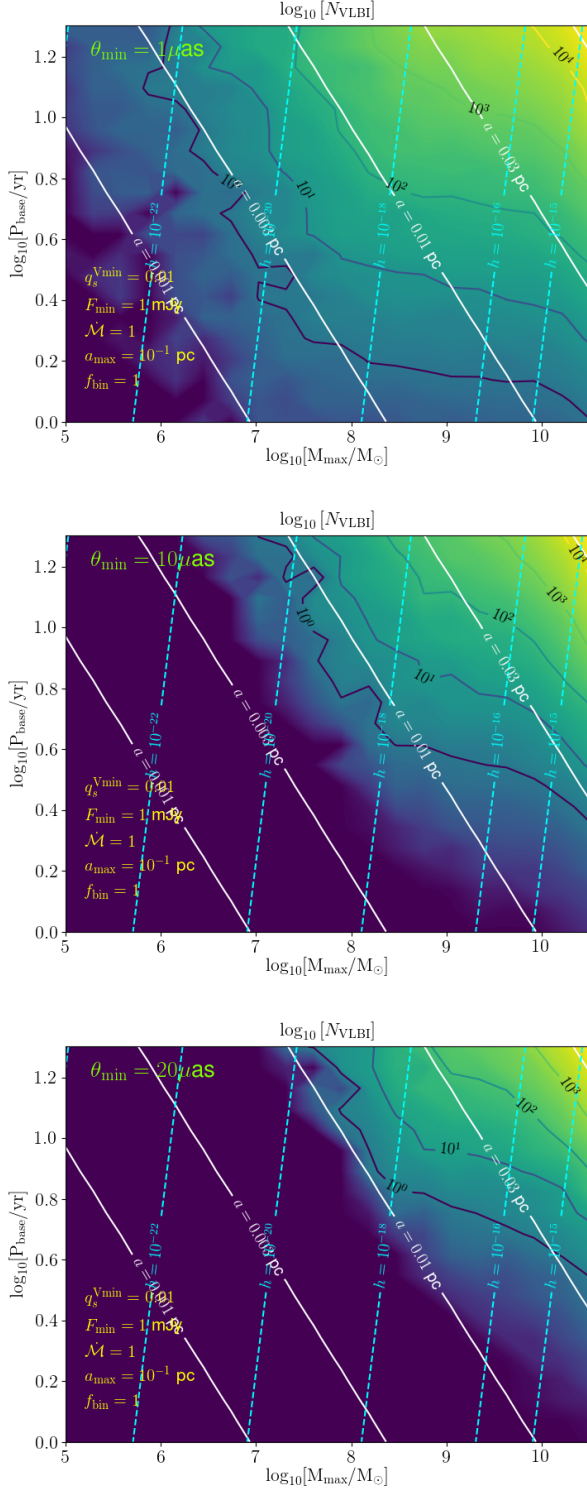


FIG. 6.— Log contours of the number of resolvable MBHBs over the entire sky, as a function of the maximum temporal baseline (maximum observed binary period) and the maximum binary mass. From top to bottom we vary the minimum angular resolution θ_{\min} from 1, to 10, to 20 μas . White lines are contours of constant binary separation. Cyan lines are contours of constant (dimensionless) gravitational-wave strain.

models can be constrained. This would provide a powerful approach to understanding the mechanisms that drive MBHBs through the final pc to centi-pc separations of their existence.

The MBHB population that can be accessed through the methods proposed here will be preferentially low Eddington ratio systems. Figure 7 shows the dependence of N_{VLBI} on the Eddington ratio in the case that f_{Edd} takes on a single value. The most striking feature of Figure 7 is the steep fall off of N_{VLBI} for $f_{\text{Edd}} \gtrsim 0.1$. As alluded to in the discussion surrounding Figure 4, this fall off is due solely to our criteria that the mm-wavelength emission region be smaller than the binary separation.

The inset of Figure 7 shows how the size of the mm-wavelength emission region grows to envelope the binary for large Eddington fractions. This inset is identical to the left-middle panel of Figure 4 except that we have plotted the integrand of Eq. (4) (labeled contours) without imposing the emission region size cut. We shade in yellow though where the cut would be enforced. These brighter MBHB systems will likely not be resolved as two point sources, however we should not preclude them as interesting targets for VLBI imaging. These circumbinary mm-emission systems could exhibit interesting morphology or time dependent behavior due to the binary orbital motion. It would be interesting if this μas morphology could be linked to larger scale jet morphology.

The inset of Figure 7 also shows that any near-Eddington sources that can be resolved as two individual sources will preferentially be low mass long period binaries. This means that the resolvable MBHB population would have a mass and period correlation with Eddington ratio.

Figure 8 shows the distribution of such circumbinary mm-emission systems assuming a single Eddington ratio of $f_{\text{Edd}} = 0.1$ and not excluding systems with mm-emission regions larger than their separation. We see that at minimum angular resolutions approaching $1\mu\text{as}$, $f_{**}f_{\text{bin}}2 \times 10^3$ of such systems could exist out to redshifts of $z \sim 0.5$. Future work should clarify what is expected from the mm-emission of these systems. It is intriguing to note that the MBHB candidates PG 1302 (Graham *et al.* 2015a) and OJ 287 (Valtonen *et al.* 2008) fall in this latter circumbinary mm-emission region category, with angular separations of $4\mu\text{as}$ and $12\mu\text{as}$, using estimated total binary masses of $10^{9.4}M_{\odot}$ and $10^{10.3}M_{\odot}$ for PG 1302 and OJ287, respectively.

5.2. Binary Mass Determination

Beyond probing the MBHB population, VLBI imaging of a MBHB orbit would allow a precise measurement of the binary mass. Consider resolving the orbital separation of a MBHB with each component active. If the binary is on a circular orbit, its separation a can be measured from the maximum resolved angular separation θ_a of the two orbiting sources and the redshift of the host galaxy $a = \theta_a D_A(z)$, where $D_A(z)$ is the angular diameter distance of the source given the redshift z . By tracking the binary for a large enough fraction of an orbit needed to fit an orbital solution (this need not be an entire orbit), the binary orbital period P can be used to measure the total mass of the binary,

$$M = \frac{1}{G} \left(\frac{2\pi}{P(1+z)} \right)^2 (\theta_a D_A(z))^3, \quad (11)$$

where the observed period is $P(1+z)$.

Assuming Gaussian errors on the measurements of P , θ_a , and comparatively negligible errors on z and the Hubble con-

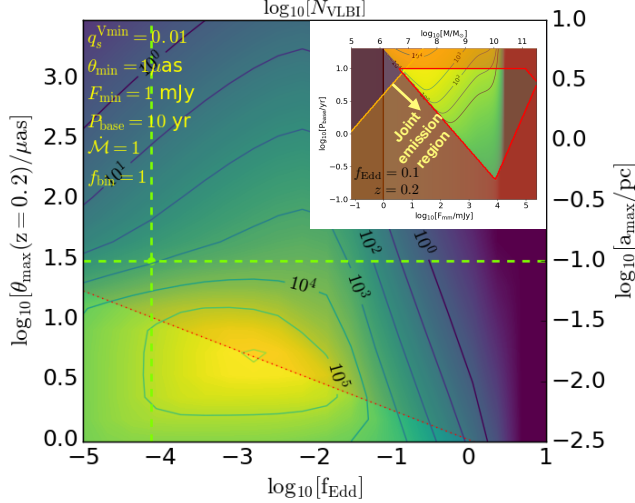


FIG. 7.— Same as the panels in Figure 5 except that the horizontal axis varies different values of a delta function distribution of the Eddington ratio f_{Edd} . The fall off in N_{VLBI} for larger f_{Edd} is due to the growing size of the mm-wavelength emission region. Only for low-Eddington fractions is the mm-emission region smaller than the characteristic binary separations considered here. The dashed-green lines mark the fiducial value of a_{max} and the expectation value of f_{Edd} from the Eddington fraction distribution (Eq. 6). The top-right inset is identical to the left-middle panel of Figure 4 but for $f_{\text{Edd}} = 0.1$ and without enforcing emission region size constraints.

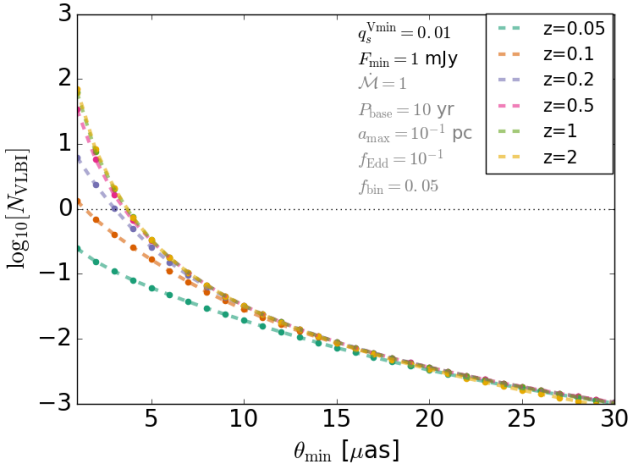


FIG. 8.— The same as the top left panel of Figure 3, except for a delta function distribution of $f_{\text{Edd}} = 0.1$ and not removing MBHBs with emission regions surrounding the binary.

stant H_0 (which factors into $D_A(z)$), the uncertainty in this mass measurement is

$$\frac{\delta M}{M} \approx \left[\left(2 \frac{\delta P}{P} \right)^2 + \left(3 \frac{\delta \theta_a}{\theta_a} \right)^2 \right]^{1/2}. \quad (12)$$

We estimate the error in the measurement of θ_a by the minimum instrument angular resolution. When we are limited by a minimum angular resolution of $\sim 10 \mu\text{as}$, the calculations of the previous section showed that most resolvable binaries are at this limiting angular separation and so $\delta \theta_a / \theta_a \sim 1$. If however, the minimum resolution can reach $\sim 1 \mu\text{as}$, we find that $\delta \theta_a / \theta_a \sim 0.1$.

From VLBI astrometry alone, the error in P is set by the cadence of observations ΔT_{obs} and also the precision at which the centroid of emission from each binary component can be

determined,

$$\delta P \approx \left[\Delta T_{\text{obs}}^2 + \left(P \frac{\theta_{\text{min}}}{\theta_a} \right)^2 \right]^{1/2}, \quad (13)$$

which in the worst case scenario can be of order P . However, as we will discuss below, identification of VLBI resolvable candidates can be carried out through searches for quasar periodicity caused either by the relativistic Doppler boost or variable circumbinary accretion. In these cases, the binary period can be identified to within a few percent (e.g. [Graham et al. 2015b](#))³. Taking into account the above best and worse case scenarios for $\delta \theta_a / \theta_a$, and a best case $\delta P / P \sim 0.05$, we estimate the precision in the MBHB mass measurement to fall between

$$0.3 \lesssim \frac{\delta M}{M} \Big|_{\text{VLBI}} \lesssim 4. \quad (14)$$

The present-day state of the art technique for measuring MBH masses, reverberation mapping, can typically measure central MBH masses to within 0.5 dex, or $\delta M / M|_{\text{RM}} \sim 3$ (e.g. [Shen 2013](#), and references therein), hence the mass measurement put forth here would rival the precision of those found through reverberation mapping techniques, and in the best case scenario provide the most precise MBH masses to date. Furthermore, the mass measurement proposed here is much cleaner in that it only requires Newtonian orbit fitting, and does not rely upon the unknown geometric factors related to AGN broad-line regions, which contribute much of the uncertainty in the reverberation mapping analysis. The mass measurements found via VLBI orbit-tracking could probe MBHBs out to redshifts of $z \sim 0.5$, in a mass range $10^6 \rightarrow 10^{10} M_{\odot}$.

5.3. Determination of the Hubble Constant

If instead there is a measurement of the central binary mass, VLBI orbit-tracking of a MBHB allows a novel measurement of the Hubble constant. This can be achieved by solving Eq. (11) for the Hubble constant, which determines $D_A(z)$. As for the mass measurement of the previous section, one must again know the redshift of the MBHB host galaxy. Using the same best case estimates for $\delta \theta_a / \theta_a \sim 0.1$ and $\delta P / P \sim 0.05$ as in the previous sub-section, and choosing an optimistic $\delta M / M \sim 0.5$, the uncertainty in the Hubble constant measured from VLBI orbit-tracking is approximately,

$$\frac{\delta H_0}{H_0} \gtrsim 0.2 \left[\left(\frac{\delta \theta_a / \theta_a}{0.1} \right)^2 + \frac{4}{9} \left(\frac{\delta P / P}{0.05} \right)^2 + \frac{1}{9} \left(\frac{\delta M / M}{0.5} \right)^2 \right]^{1/2}, \quad (15)$$

down to 20% relative error. If the relative error in θ_a and M could be decreased to 5%, the measurement uncertainty in H_0 would drop to 6%.

If the binary generates periodically variable continuum emission due to the relativistic Doppler boost ([D’Orazio et al. 2015b](#)), then simultaneous VLBI monitoring of MBHB astrometry and Doppler-boosted fluxes can determine the Hubble constant even without a binary mass measurement.

³ The strongest observed periodicity could be higher or lower than the orbital period ([Charisi et al. 2015](#); [D’Orazio et al. 2015a](#)), but in each scenario, the true orbital period could still be discernible with a long enough observation.

For the range of binary periods and masses for which we predict more than one resolvable MBHB (e.g., the left panel of Figure 6), the orbital velocity can range from $\sim 0.01c$, for $M \sim 10^7 M_\odot$ and $P \sim 10$ yrs, up to $\sim 0.19c$ for $M \sim 10^{10} M_\odot$ and $P \sim 1.5$ yrs, meaning that significant Doppler modulation, at the tens of percent level, is possible.

Assume again that we have observations of a resolved MBHB with both MBHs active. Then mm-VLBI can observe the orbital motion projected on to the sky. The observed angular velocity of the i^{th} binary component is,

$$\dot{\theta}_i = (1+z) \frac{v_i(q)}{D_A(z)} \sqrt{\cos^2 [\Omega t] \sin^2 I + \sin^2 [\Omega t]}, \quad (16)$$

where I is the inclination of the binary orbital plane to the line of sight, $\Omega = 2\pi/P$ is the observed angular orbital frequency of the binary, and v_i is the rest frame orbital velocity of the i^{th} MBH. We assume a binary with mass ratio q on a circular orbit,

$$v_p = \frac{q}{1+q} \left(\frac{GM\Omega}{1+z} \right)^{1/3} = qv_s, \quad (17)$$

where s denotes secondary and p denotes primary, and

$$D_A(z) = \frac{c}{H_0(1+z)} \int_0^z \frac{dz'}{\sqrt{\Omega_M(1+z')^3 + \Omega_\Lambda}} \quad (18)$$

is the angular diameter distance of the source at redshift z

for Hubble constant H_0 , and matter and dark energy density parameters Ω_M and Ω_Λ .

If the binary is on a circular orbit, the inclination of the binary can be discerned from the projected shape of the orbit alone. The inclination can also be recovered for an eccentric orbit. However, the change in proper motion along the path of the eccentric orbit must also be included to break the degeneracy between, for example, a face on elliptical orbit and a tilted circular orbit. Assuming a circular orbit for simplicity of demonstration,

$$I = \tan^{-1} \left(\frac{\theta^b}{\theta^a} \right), \quad (19)$$

where θ^a and θ^b are the semi-major and semi-minor axes of the ellipse that the binary orbital motion traces. In the more general case, tracking the proper motion of the binary components will allow measurement of the orbital eccentricity.

Similarly, the mass ratio could be measured if the binary orbit is resolved on the sky. For example, a binary on a circular orbit with semi-major axis a , has a secondary that orbits at a distance $r_s = a/(1+q)$ from the binary center of mass while the primary orbits at a distance $r_p = aq/(1+q)$. The measurement of the ratio of these angular distances yields the binary mass ratio.

The orbital velocity can be measured independently from monitoring the periodically changing flux caused by the relativistic Doppler boost. Generally, the emission from both MBHs must be taken into account,

$$\begin{aligned} \frac{F_\nu^{\text{obs}}}{F_\nu^0}(t) &= f_s \left[\gamma_s \left(1 - \frac{v_{s||}}{c} \right) \right]^{\alpha-3} + (1-f_s) \left[\gamma_p \left(1 + q \frac{v_{s||}}{c} \right) \right]^{\alpha-3} \\ v_{s||} &= v_s \cos [\Omega t] \cos I; \quad \gamma_i = \left[1 - \left(\frac{v_i}{c} \right)^2 \right]^{-1/2}, \end{aligned} \quad (20)$$

where $||$ denotes the velocity component along the line of sight and we have used that $v_{p||} = -qv_{s||}$. This introduces a new quantity $f_s = \langle F_s / (F_s + F_p) \rangle$, the fraction of time averaged flux detected from the secondary compared to the total. From measurements of α , I , q , and the time dependent flux, we solve the above equation for the orbital velocity of the secondary and primary MBH.

Hence, the two measurements of the Hubble constant are given by

$$(H_0)_i = \frac{c\dot{\theta}_i \int_0^z \frac{dz'}{\sqrt{\Omega_M(1+z')^3 + \Omega_\Lambda}}}{v_i \sqrt{\cos^2 [\Omega t] \sin^2 I + \sin^2 [\Omega t]}}. \quad (21)$$

which must be averaged over some fraction of the binary orbit in order to measure $\dot{\theta}_i$. This measurement of H_0 could then be used in conjunction with the method using Eq. (11) to further improve the uncertainty in the VLBI-measured Hubble constant.

Note that this method for measuring the Hubble constant with proper motions and orbital velocities can also be carried out without detection of the Doppler boost, but with a measurement of the binary mass and mass ratio. In this case, the

orbital velocity of each MBH yields via Eq. (17).

As an example for the precision at which the Hubble constant can be measured in the Doppler-boost method, we envision the simplest case. We consider the case where only the Doppler boost from the secondary is important and where $\gamma_s \sim 1$.⁴ Then the secondary orbital velocity can be written as,

$$\begin{aligned} \frac{v_s}{c} \cos I &= [\Delta_+ + 1]^{\frac{1}{\alpha-3}} - 1 \\ \Delta_+ &\equiv \frac{F_\nu^{\text{obs}}(0)}{F_\nu^0} - \frac{F_\nu^{\text{obs}}(P/4)}{F_\nu^0}, \end{aligned} \quad (22)$$

where the Δ_+ is the modulation amplitude between peak and average flux (between $t = 0$ and $t = P/4$). Assuming that uncertainty in the binary inclination dominates, we can write $\delta v/v \approx I \tan I (\delta I/I)$. Assuming a small inclination angle to the line of sight (needed for the Doppler boost to be significant), we approximate $I \sim \theta_b/\theta_a$ (from Eq. 19), and $\delta I/I \approx \sqrt{2}(\delta\theta_a/\theta_a)$. Taking optimistic values of $I \leq 0.5$

⁴ This applies, for example, in the case that VLBI can isolate emission from one of the binary components, or when the mass ratio is disparate and only the secondary contributes strongly to the Doppler boost.

rad, $\delta\dot{\theta}/\dot{\theta} = 0.1$, $\delta\theta_a/\theta_a = 0.1$, and $\delta\Omega/\Omega = 0.05$,

$$\frac{\delta H_0}{H_0} \gtrsim 0.1 \quad (\text{Doppler case}), \quad (23)$$

which is valid for $I \leq 0.5$, where this estimate does not vary greatly over the course of the orbit. If these measurements can be made out to redshifts $z > 0.1$, as Figure 3 suggests is possible, then they could provide an independent measure of the Hubble constant that could aid in resolving discrepancies in other independent measurements such as the current mismatch between H_0 measured by Planck via the cosmic microwave background (Planck Collaboration *et al.* 2016), and the value measured by the Hubble space telescope via the Cepheid variables (Riess *et al.* 2016).

5.4. Observational Strategy

As mm-VLBI is not suited for all-sky surveys, we require pilot observations that can identify MBHB mm-bright candidates for VLBI follow up. We have shown that the majority of resolvable MBHBs would be at the heart of mm-bright LLAGN. This means that there will be only a dim optical/UV component to these sources, (LLAGN do not exhibit a big-blue bump in their spectra). LLAGN spectra, however, are brighter in the near-IR (*e.g.* Fernández-Ontiveros *et al.* 2012) and hence accessible via upcoming time-domain surveys such as the Large Synoptic Survey Telescope (LSST; Ivezić and *et al.* 2008). Hence we propose the following general strategy to find VLBI MBHB candidates:

1. Search for periodicity with all-sky time domain surveys in the near-IR, *e.g.*, LSST. Such a survey will identify a list of MBHB candidates from which we can select those with the required binary separations given a mass estimator and the observed variability period (see *e.g.*, Graham *et al.* 2015b; Charisi *et al.* 2016). We note that the lifetime of these surveys will set the size of the maximum binary period P_{base} . Currently, surveys such as the Catalina Real Time Transient Survey have a 10 year temporal baseline (Djorgovski *et al.* 2011).
2. Determine whether each periodic-light-curve candidate is radio loud (and hence bright in mm-wavelengths), either via archival searches or follow up with single radio observations.
3. Observe candidates that pass stages 1 and 2 with mm-VLBI and determine if they consist of two compact sources, or one compact source and a nearby phase calibrator. If they do, monitor these sources for orbital motion. Even for the longest period binaries considered here (10 years), two or three observations spaced by a year would be sufficient to test for orbital motion.

We point out that an advantage to searching for sub-pc separation, dual-source binaries, over searching for wide, pc-kpc dual AGN, is that these smaller separation binaries could be identified for follow-up via the imprint of their orbital period.

5.5. Gravitational wave single-source detection

As shown in the cyan contours of Figure 6, the nearest MBHBs at the high mass and low period end of the resolvable population could be detectable as single GW sources⁵. In this

⁵ See Schutz and Ma (2016) for constraints on the mass-ratios of a nearby, most-massive population of putative MBHBs.

case, the EM discovery of a MBHB could aid the PTAs in digging out a weak signal of the binary. Such identification could also allow a precision binary mass measurement that could be used to increase the precision of the Hubble constant measurement of §5.3, or to corroborate the mass measurement of §5.2. A simultaneous GW detection could also contribute a second, independent measurement of the Hubble constant through the standard sirens approach (see Schutz 1986; Abbott *et al.* 2017, and references therein).

Finally, VLBI orbit-tracking plus GW detection of a MBHB could be used to measure the relative speed of light and GWs. This can be achieved by tracking the binary orbital phase through both the EM and GW messengers. The detection of the relativistic Doppler boost would further enhance the capability to make such a measurement (see Haïman 2017, for a similar scenario).

6. CONCLUSIONS AND FUTURE WORK

By constructing simple models for gas and gravitational-wave-driven binary orbital decay and a mm-wavelength AGN luminosity function, we estimate the number of MBHBs, over the entire sky, that reside at separations directly resolvable by mm-wavelength VLBI, and with orbital periods of less than 10 years. We show that, $1 - 10\mu\text{s}$ resolution, sub-mm VLBI with flux sensitivity better than 1 mJy can resolve the orbital separation of tens of MBHBs at fiducial model parameters, and up to $\sim 10^4$ at parameter values tuned to maximize this number. These MBHBs are found out to redshift $z \approx 0.5$ and have total masses above $\sim 10^7 M_\odot$.

For a minimum flux sensitivity of 10mJy, closer to current capabilities, there are of order a few resolvable MBHBs out to redshift $z \lesssim 0.2$. For an enhanced sub-mm flux sensitivity of 0.1mJy, our fiducial MBHB-decay model predicts that a few $\times 10^2$ MBHBs will be resolvable at $1\mu\text{s}$ resolution out to $z \lesssim 1.0$, while of order one MBHB will be resolvable with $25\mu\text{s}$ resolution. Further extending the maximum temporal baseline to include 20 year binary orbital periods increases the all-sky number of resolvable MBHBs to a few thousand at the best case $1\mu\text{s}$ resolution, and a few tens even at a minimum angular resolution of $30\mu\text{as}$.

We determine that resolvable MBHBs, for which each component is tracked by a mm-emission region smaller than the binary orbit, preferentially reside in low-luminosity AGN. These objects could be identified through periodicity signatures in near-IR/optical time domain surveys and followed up with radio observations as a precursor for VLBI orbit-tracking.

Resolvable MBHBs will be emitting gravitational radiation in the PTA band ($\sim\text{nHz}$). If they are within a redshift of 0.1, the closest, most massive MBHBs could be detectable as individual binary sources. We show that the total binary fraction of these low-luminosity AGN is constrained to be $\lesssim 0.05$ by PTA limits on the gravitational wave background.

Beyond providing definitive existence of sub-pc MBHBs, VLBI tracking of a complete binary orbit would allow a measurement of the binary mass (to within $\sim 30\%$), or a novel, $\mathcal{O}(10\%)$, measurement of the Hubble constant, if the binary mass is known.

Future work should consider improved models for the orbital decay of MBHBs and their mm-bright lifetimes. This is important for understanding the range in predictions for the number of resolvable MBHBs and also for determining how well such models can be ruled out by future population estimates. Additionally, future work should understand the pop-

ulation of periodic-light-curve candidates that could be identified with current and future time domain surveys, specifically, the subset of these that are VLBI imaging candidates. Further analysis of the existing MBHB candidates in the literature may already provide interesting targets for VLBI orbit tracking. For example, PG 1302-102, OJ 287, and 3C 273 are each sub-mm bright AGN within redshift 0.3 that have been reported as MBHB candidates with observed periods of 5, 12, and 16 years (Graham *et al.* 2015a; Valtonen *et al.* 2008; Abraham and Romero 1999; Romero *et al.* 2000) respectively. From total binary mass estimates of $10^{9.4} M_\odot$, $10^{10.3} M_\odot$, and $10^9 M_\odot$, this corresponds to putative angular separations of the binary orbits of 4, 12, and $10 \mu\text{as}$.

The authors thank the referee, Zoltán Haiman, for a very insightful and thorough review which greatly enhanced the clarity of this work. The authors also thank Eliot Quataert, Michael Johnson, Lindy Blackburn, Sheperd Doeleman, Michael Eracleous, Atish Kamble, Bence Kocsis, Anna Pancoast, and Mark Reid for useful discussions. Financial support was provided from NASA through Einstein Postdoctoral Fellowship award number PF6-170151 (DJD) and through the Black Hole Initiative which is funded by a grant from the John Templeton Foundation.

APPENDIX

MILLIMETER-WAVELENGTH AGN LUMINOSITY FUNCTION

We use a redshift dependent luminosity function of radio-loud AGN that takes into account both density evolution and luminosity evolution (Yuan *et al.* 2017),

$$\begin{aligned} \frac{d^2 N}{dL dV} &= e_1(z) \frac{\phi}{L_{408}/e_2(z) \ln 10} \left(\frac{L_{408}/e_2(z)}{L_*} \right)^{-\beta} \exp \left[-\frac{L_{408}/e_2(z)}{L_*} \right] \\ e_1(z) &= \frac{(1+z_c)^{-p_1} + (1+z_c)^{-p_2}}{\left(\frac{1+z}{1+z_c}\right)^{p_1} + \left(\frac{1+z}{1+z_c}\right)^{p_2}}, \quad e_2(z) = 10^{k_1 z + k_2 z^2}, \\ L_* &= 10^{24.79} \text{WHz}^{-1}, \quad \phi = 10^{-4.72} \text{Mpc}^{-3}, \quad p_1 = -1.29, \quad p_2 = 6.80, \\ \beta &= 0.45, \quad \gamma = 0.31, \quad k_1 = 1.44 \quad k_2 = -0.16, z_c = 0.78, \end{aligned} \quad (\text{A1})$$

where L_{408} is the specific luminosity at 408 MHz. This is scaled to a mm-wavelength luminosity function as described in the main text. We note for ease of reproducibility, that in Table 1 of (Yuan *et al.* 2017) the values of k_1 and k_2 are erroneously swapped while the values of p_1 and p_2 are erroneously stated as their negatives (needed to reproduce Figures 3 and 4 in Yuan *et al.* (2017)).

THE SIZE OF THE MM-WAVELENGTH EMISSION REGION IN LLAGN

We require that the size of the mm-wavelengths emission region be smaller than the binary separation. We estimate the size of the mm-emission region with the jet model of (Blandford and Königl 1979).

The radio and mm-emission from MBHBs is likely from synchrotron emission generated by shocks in a jet. At low frequencies, synchrotron radiation is optically thick to self absorption and its spectrum rises as $F_\nu^{\text{thick}} \propto \nu^{5/2}$ until the radiation becomes optically thin at frequency ν_{ssa} . For higher frequencies the optically thin spectrum falls off as $F_\nu^{\text{thin}} \propto$

$\nu^{-(p-1)/2}$ where the electrons are assumed to be distributed as $N_e = K_e \gamma_e^{-p}$. At even higher frequencies, however, the synchrotron losses are great enough to cool the radiation within a jet expansion time. Then above some ν_{loss} , the synchrotron flux drops more steeply as $F_\nu^{\text{loss}} \propto \nu^{-(p-1)/2-0.5}$.

Both limiting frequencies, and hence the shape of the synchrotron spectrum, depends on radial position within the jet. The self absorption frequency ν_{ssa} , for which only higher frequency synchrotron photons can escape becomes larger at larger radii in the jet. The maximum frequency for which synchrotron losses are negligible, ν_{loss} , decreases with radius in the jet. Hence, there is a minimum jet radius r_{min} below which no bright, optically thin synchrotron spectrum exists. This minimum radius is given by equating $\nu_{ssa}(r) = \nu_{\text{loss}}(r)$.

Then for the mm-emission regions to be smaller than the binary separation, we must have, $\nu_{ssa}(a) < \nu_{mm} < \nu_{\text{loss}}(a)$. In practice we evaluate this inequality for a given binary separation a and set the resolvable MBHB probability \mathcal{F} equal to zero if it is not satisfied.

The self absorption frequency is given by (Eq. 28 of Blandford and Königl 1979),

$$\nu_{ssa} = \frac{300}{1+z} k_e^{1/3} \left[\Delta \left(1 + \frac{2}{3} k_e \Lambda \right) \right]^{-2/3} \gamma_j^{-4/3} \beta_j^{-2/3} D_j^{2/3} (\sin \theta)^{-1/3} \phi_{\text{ob}}^{-1} L_{44}^{2/3} \left(\frac{r_{\text{ob}}}{0.01 \text{pc}} \right)^{-1} \text{GHz}, \quad (\text{B1})$$

where $k_e \lesssim 1$, Δ is the logarithm of the ratio of maximum and minimum size scales in the jet, Λ is the logarithm of the ratio of maximum and minimum electron Lorentz factors in the jet, $\gamma_j = (1 - \beta_j^2)^{-1/2}$ is the Lorentz factor of the jet, D_j is the jet Doppler factor, θ is the viewing angle of the jet, $\phi_{\text{ob}} = \phi / \sin \theta$ is the observed opening angle of the jet, L_{44} is the bolometric luminosity of the jet in units of $10^{44} \text{erg s}^{-1}$, and $r_{\text{ob}} = r \sin \theta$ is the observed distance from jet launching point to the emission

region. This suggests that sources with $L \sim 10^{44} \text{ erg s}^{-1}$ are optically thin at mm-wavelengths down to size scales of $r \sim 0.01 \text{ pc}$. Lower luminosity sources are visible down to even smaller scales.

The maximum frequency for which synchrotron losses are negligible,

$$\nu_{\text{loss}} = \frac{0.07}{1+z} \gamma_j^2 \beta_j^2 \frac{D_j}{\sin \theta B_1^3} r_{\text{ob}}, \quad (\text{B2})$$

where B_1 is the magnetic field strength at $r = 1 \text{ pc}$,

$$B_1 = 2 \left[\Delta \left(1 + \frac{2}{3} k_e \Lambda \right) \right]^{-1/2} \phi(\beta_j c)^{-1/2} \gamma_j \left(\frac{r}{1 \text{ pc}} \right)^{-1} \left(\frac{L}{10^{44} \text{ erg s}^{-1}} \right)^{1/2}, \quad (\text{B3})$$

is found by equating the total power in the jet to that carried away by relativistic electrons and the magnetic field (Eq. 23 of Blandford and Königl 1979).

Throughout we use $k_e = 1$, $\Delta = \Lambda = \ln(10^5)$, $\gamma_j = 10$, $\phi = 1/\gamma_j$, and $\theta = 0.1$. The choice of θ is conservative as it yields the maximum value of ν_{ssa} .

REFERENCES

- J. Kormendy and D. Richstone, *ARA&A* **33**, 581 (1995).
 G. Kauffmann and M. Haehnelt, *MNRAS* **311**, 576 (2000).
 L. Ferrarese and H. Ford, *SSR* **116**, 523 (2005).
 J. Kormendy and L. C. Ho, *ARA&A* **51**, 511 (2013), arXiv:1304.7762.
 M. Colpi and M. Dotti, *Advanced Science Letters* **4**, 181 (2011).
 S. Callegari, S. Kazantzidis, L. Mayer, M. Colpi, J. M. Bellovary, T. Quinn, and J. Wadsley, *ApJ* **729**, 85 (2011), arXiv:1002.1712 [astro-ph.CO].
 L. Mayer, *Classical and Quantum Gravity* **30**, 244008 (2013), arXiv:1308.0431.
 F. Dosopoulou and F. Antonini, ArXiv e-prints (2016), arXiv:1611.06573.
 M. C. Begelman, R. D. Blandford, and M. J. Rees, *Nature* **287**, 307 (1980).
 D. Merritt and M. Milosavljević, *Living Reviews in Relativity* **8** (2005).
 M. Milosavljević and D. Merritt, *THE ASTROPHYSICS OF GRAVITATIONAL WAVE SOURCES*. AIP Conference Proceedings **686**, 201 (2003).
 A. Gould and H.-W. Rix, *ApJL* **532**, L29 (2000), astro-ph/9912111.
 P. J. Armitage and P. Natarajan, *ApJL* **567**, L9 (2002).
 Y. Tang, A. MacFadyen, and Z. Haiman, ArXiv e-prints (2017), arXiv:1703.03913 [astro-ph.HE].
 F. G. Goicovic, A. Sesana, J. Cuadra, and F. Stasyszyn, ArXiv e-prints (2016), arXiv:1602.01966 [astro-ph.HE].
 A. Gualandris, J. I. Read, W. Dehnen, and E. Bortolas, *MNRAS* **464**, 2301 (2017), arXiv:1609.09383.
 Z. Haiman, B. Kocsis, and K. Menou, *ApJ* **700**, 1952 (2009).
 S. Komossa, *Memorie della Società Astronomica Italiana* **77**, 733 (2006).
 C. Rodriguez, G. B. Taylor, R. T. Zavala, A. B. Peck, L. K. Pollack, and R. W. Romani, *The Astrophysical Journal* **646**, 49 (2006).
 S. Burke-Spolaor, *Monthly Notices of the Royal Astronomical Society* **410**, 2113 (2011).
 G. Fabbiano, J. Wang, M. Elvis, and G. Risaliti, *Nature* **477**, 431 (2011).
 M. Dotti, A. Sesana, and R. Decarli, *Advances in Astronomy* **2012**, 940568 (2012), arXiv:1111.0664 [astro-ph.CO].
 F. Civano, M. Elvis, G. Lanzuisi, T. Aldcroft, M. Trichas, A. Bongiorno, M. Brusa, L. Blecha, A. Comastri, A. Loeb, M. Salvato, A. Fruscione, A. Koekemoer, S. Komossa, R. Gilli, V. Mainieri, E. Piconcelli, and C. Vignali, *ApJ* **752**, 49 (2012), arXiv:1205.0815.
 L. Blecha, F. Civano, M. Elvis, and A. Loeb, *MNRAS* **428**, 1341 (2013), arXiv:1205.6202.
 J. M. Comerford, K. Schluns, J. E. Greene, and R. J. Cool, *ApJ* **777**, 64 (2013), arXiv:1309.2284.
 J.-H. Woo, H. Cho, B. Husemann, S. Komossa, D. Park, and V. N. Bennert, *Monthly Notices of the Royal Astronomical Society* **437**, 32 (2014).
 A. N. Lommen, *Journal of Physics Conference Series* **363**, 012029 (2012).
 R. N. Manchester and IPTA, *Classical and Quantum Gravity* **30**, 224010 (2013), arXiv:1309.7392 [astro-ph.IM].
 M. A. McLaughlin, *Classical and Quantum Gravity* **30**, 224008 (2013), arXiv:1310.0758 [astro-ph.IM].
 M. Kramer and D. J. Champion, *Classical and Quantum Gravity* **30**, 224009 (2013).
 G. Hobbs, *Classical and Quantum Gravity* **30**, 224007 (2013), arXiv:1307.2629 [astro-ph.IM].
 R. M. Shannon, V. Ravi, L. T. Lentati, P. D. Lasky, G. Hobbs, M. Kerr, R. N. Manchester, W. A. Coles, Y. Levin, M. Bailes, N. D. R. Bhat, S. Burke-Spolaor, S. Dai, M. J. Keith, S. Osłowski, D. J. Reardon, W. van Straten, L. Toomey, J.-B. Wang, L. Wen, J. S. B. Wyithe, and X.-J. Zhu, *Science* **349**, 1522 (2015), arXiv:1509.07320.
 L. Z. Kelley, L. Blecha, L. Hernquist, and A. Sesana, ArXiv e-prints (2017a), arXiv:1702.02180 [astro-ph.HE].
 J. E. Barnes and L. Hernquist, *ApJ* **471**, 115 (1996).
 J. E. Barnes, *MNRAS* **333**, 481 (2002), astro-ph/0201250.
 Y. Shen and A. Loeb, *ApJ* **725**, 249 (2010), arXiv:0912.0541 [astro-ph.CO].
 P. Tsalmantza, R. Decarli, M. Dotti, and D. W. Hogg, *ApJ* **738**, 20 (2011).
 T. Bogdanović, M. Eracleous, and S. Sigurdsson, *NewAR* **53**, 113 (2009a), arXiv:0909.0516.
 M. Eracleous, T. A. Boroson, J. P. Halpern, and J. Liu, *ApJS* **201**, 23 (2012), arXiv:1106.2952.
 B. McKernan, K. E. S. Ford, B. Kocsis, and Z. Haiman, *MNRAS* **432**, 1468 (2013).
 R. Decarli, M. Dotti, M. Fumagalli, P. Tsalmantza, C. Montuori, E. Lusso, D. W. Hogg, and J. X. Prochaska, *MNRAS* **433**, 1492 (2013), arXiv:1305.4941.
 Y. Shen, X. Liu, A. Loeb, and S. Tremaine, *ApJ* **775**, 49 (2013), arXiv:1306.4330.
 X. Liu, Y. Shen, F. Bian, A. Loeb, and S. Tremaine, *ApJ* **789**, 140 (2014a), arXiv:1312.6694.
 J. Liu, M. Eracleous, and J. P. Halpern, *ApJ* **817**, 42 (2016), arXiv:1512.01825 [astro-ph.HE].
 F. K. Liu, S. Li, and X. Chen, *ApJL* **706**, L133 (2009), arXiv:0910.4152 [astro-ph.HE].
 N. Stone and A. Loeb, *MNRAS* **412**, 75 (2011), arXiv:1004.4833.
 E. R. Coughlin, P. J. Armitage, C. Nixon, and M. C. Begelman, *MNRAS* **465**, 3840 (2017), arXiv:1608.05711.
 A. C. Gower, P. C. Gregory, W. G. Unruh, and J. B. Hutchings, *ApJ* **262**, 478 (1982).
 N. Roos, J. S. Kaastra, and C. A. Hummel, *ApJ* **409**, 130 (1993).
 D. Merritt and R. D. Ekers, *Science* **297**, 1310 (2002), astro-ph/0208001.
 C. Zier and P. L. Biermann, *A&A* **396**, 91 (2002).
 G. E. Romero, L. Chajet, Z. Abraham, and J. H. Fan, *A&A* **360**, 57 (2000).
 E. Kun, K. É. Gabányi, M. Karouzos, S. Britzen, and L. Á. Gergely, *MNRAS* **445**, 1370 (2014), arXiv:1402.2644 [astro-ph.HE].
 E. Kun, S. Frey, K. É. Gabányi, S. Britzen, D. Cseh, and L. Á. Gergely, *MNRAS* **454**, 1290 (2015), arXiv:1506.07036 [astro-ph.HE].
 G. Kulkarni and A. Loeb, *MNRAS* **456**, 3964 (2016), arXiv:1507.06990.
 H. Sudou, S. Iguchi, Y. Murata, and Y. Taniguchi, *Science* **300**, 1263 (2003), astro-ph/0306103.
 K. Hayasaki and S. Mineshige, *ORIGIN OF MATTER AND EVOLUTION OF GALAXIES: The 10th International Symposium on Origin of Matter and Evolution of Galaxies: From the Dawn of Universe to the Formation of Solar System*. AIP Conference Proceedings **1016**, 406 (2008).
 D. J. D'Orazio, Z. Haiman, and A. MacFadyen, *MNRAS* **436**, 2997 (2013).
 D. J. D'Orazio, Z. Haiman, P. Duffell, B. D. Farris, and A. I. MacFadyen, *MNRAS* **452**, 2540 (2015a), arXiv:1502.03112 [astro-ph.HE].
 B. D. Farris, P. Duffell, A. I. MacFadyen, and Z. Haiman, *ApJ* **783**, 134 (2014), arXiv:1310.0492 [astro-ph.HE].

- D. J. D’Orazio and R. Di Stefano, ArXiv e-prints (2017), [arXiv:1707.02335 \[astro-ph.HE\]](#).
- T. Bogdanović, M. Eracleous, and S. Sigurdsson, *ApJ* **697**, 288 (2009b), [arXiv:0809.3262](#).
- M. J. Valtonen, H. J. Lehto, K. Nilsson, J. Heidt, L. O. Takalo, A. Sillanpää, C. Villforth, M. Kidger, G. Poyner, T. Pursimo, S. Zola, J.-H. Wu, X. Zhou, K. Sadakane, M. Drozd, D. Koziel, D. Marchev, W. Ogloza, C. Porowski, M. Siwak, G. Stachowski, M. Winiarski, V.-P. Hentunen, M. Nissinen, A. Liakos, and S. Dogru, *Nature* **452**, 851 (2008), [arXiv:0809.1280](#).
- F. K. Liu, S. Li, and S. Komossa, *ApJ* **786**, 103 (2014b), [arXiv:1404.4933 \[astro-ph.HE\]](#).
- M. J. Graham, S. G. Djorgovski, D. Stern, E. Glikman, A. J. Drake, A. A. Mahabal, C. Donalek, S. Larson, and E. Christensen, *Nature* **518**, 74 (2015a), [arXiv:1501.01375](#).
- Y.-R. Li, J.-M. Wang, Z.-X. Zhang, K. Wang, Y.-K. Huang, K.-X. Lu, C. Hu, P. Du, L. C. Ho, J.-M. Bai, W.-H. Bian, and Y.-F. Yuan, ArXiv e-prints (2017), [arXiv:1705.07781 \[astro-ph.HE\]](#).
- M. J. Graham, S. G. Djorgovski, D. Stern, A. J. Drake, A. A. Mahabal, C. Donalek, E. Glikman, S. Larson, and E. Christensen, *MNRAS* **453**, 1562 (2015b), [arXiv:1507.07603](#).
- M. Charisi, I. Bartos, Z. Haiman, A. M. Price-Whelan, M. J. Graham, E. C. Bellm, R. R. Laher, and S. Marka, ArXiv e-prints (2016), [arXiv:1604.01020](#).
- K. Akiyama, K. Kuramochi, S. Ikeda, V. L. Fish, F. Tazaki, M. Honma, S. S. Doeleman, A. E. Broderick, J. Dexter, M. Mościbrodzka, K. L. Bouman, A. A. Chael, and M. Zaizen, *ApJ* **838**, 1 (2017a), [arXiv:1702.07361 \[astro-ph.IM\]](#).
- K. Akiyama, S. Ikeda, M. Pleau, V. L. Fish, F. Tazaki, K. Kuramochi, A. E. Broderick, J. Dexter, M. Mościbrodzka, M. Gowanlock, M. Honma, and S. S. Doeleman, *AJ* **153**, 159 (2017b), [arXiv:1702.00424 \[astro-ph.IM\]](#).
- S. S. Doeleman, J. Weintroub, A. E. E. Rogers, R. Plambeck, R. Freund, R. P. J. Tilanus, P. Friberg, L. M. Ziurys, J. M. Moran, B. Corey, K. H. Young, D. L. Smythe, M. Titus, D. P. Marrone, R. J. Cappallo, D. C.-J. Bock, G. C. Bower, R. Chamberlin, G. R. Davis, T. P. Krichbaum, J. Lamb, H. Maness, A. E. Niell, A. Roy, P. Strittmatter, D. Werthimer, A. R. Whitney, and D. Woody, *Nature* **455**, 78 (2008), [arXiv:0809.2442](#).
- A. E. Broderick, A. Loeb, and M. J. Reid, *ApJ* **735**, 57 (2011), [arXiv:1104.3146 \[astro-ph.HE\]](#).
- M. Elvis, F. J. Lockman, and C. Fassnacht, *ApJS* **95**, 413 (1994).
- A. L. Strom, A. Siemiginowska, M. A. Gurwell, and B. C. Kelly, ArXiv e-prints (2010), [arXiv:1001.0806 \[astro-ph.HE\]](#).
- G. C. Bower, J. Dexter, S. Markoff, M. A. Gurwell, R. Rao, and I. McHardy, *ApJL* **811**, L6 (2015), [arXiv:1508.06603 \[astro-ph.HE\]](#).
- C. L. MacLeod, Ž. Ivezić, C. S. Kochanek, S. Kozłowski, B. Kelly, E. Bullock, A. Kimball, B. Sesar, D. Westman, K. Brooks, R. Gibson, A. C. Becker, and W. H. de Vries, *ApJ* **721**, 1014 (2010), [arXiv:1004.0276 \[astro-ph.CO\]](#).
- R. D. Blandford and A. Königl, *ApJ* **232**, 34 (1979).
- P. F. Hopkins, K. Bundy, L. Hernquist, and R. S. Ellis, *ApJ* **659**, 976 (2007a), [astro-ph/0601621](#).
- P. Martini, Coevolution of Black Holes and Galaxies, 169 (2004), [astro-ph/0304009](#).
- P. F. Hopkins, A. Lidz, L. Hernquist, A. L. Coil, A. D. Myers, T. J. Cox, and D. N. Spergel, *ApJ* **662**, 110 (2007b), [astro-ph/0611792](#).
- P. C. Peters, *Physical Review* **136**, 1224 (1964).
- A. Loeb, *PRD* **81**, 047503 (2010), [arXiv:0909.0261 \[astro-ph.CO\]](#).
- R. R. Rafikov, arXiv.org, [arXiv:1602.05206](#) (2016), [1602.05206](#).
- R. Miranda, D. J. Muñoz, and D. Lai, *MNRAS* **466**, 1170 (2017), [arXiv:1610.07263 \[astro-ph.SR\]](#).
- J. Goodman, *MNRAS* **339**, 937 (2003).
- D. W. Hogg, ArXiv Astrophysics e-prints (1999), [astro-ph/9905116](#).
- G. Kauffmann and T. M. Heckman, *MNRAS* **397**, 135 (2009), [arXiv:0812.1224](#).
- F. Shankar, D. H. Weinberg, and J. Miralda-Escudé, *MNRAS* **428**, 421 (2013), [arXiv:1111.3574](#).
- A. K. Weigel, K. Schawinski, N. Caplar, O. I. Wong, E. Treister, and B. Trakhtenbrot, *ApJ* **845**, 134 (2017), [arXiv:1707.05323](#).
- M. Eracleous, J. A. Hwang, and H. M. L. G. Flohic, *ApJS* **187**, 135 (2010), [arXiv:1001.2924](#).
- J. A. Fernández-Ontiveros, M. A. Prieto, J. A. Acosta-Pulido, and M. Montes, in *Journal of Physics Conference Series*, Journal of Physics Conference Series, Vol. 372 (2012) p. 012006, [arXiv:1206.0777](#).
- M. J. Reid and M. Honma, *ARA&A* **52**, 339 (2014), [arXiv:1312.2871 \[astro-ph.IM\]](#).
- E. S. Phinney, ArXiv Astrophysics e-prints (2001), [astro-ph/0108028](#).
- A. Sesana, A. Vecchio, and C. N. Colacino, *MNRAS* **390**, 192 (2008), [arXiv:0804.4476](#).
- B. Kocsis and A. Sesana, *MNRAS* **411**, 1467 (2011), [arXiv:1002.0584](#).
- A. Sesana, Z. Haiman, B. Kocsis, and L. Z. Kelley, ArXiv e-prints (2017), [arXiv:1703.10611 \[astro-ph.HE\]](#).
- L. Z. Kelley, L. Blecha, and L. Hernquist, *MNRAS* **464**, 3131 (2017b), [arXiv:1606.01900 \[astro-ph.HE\]](#).
- C. M. F. Mingarelli, T. J. W. Lazio, A. Sesana, J. E. Greene, J. A. Ellis, C.-P. Ma, S. Croft, S. Burke-Spolaor, and S. R. Taylor, *Nature Astronomy* **1**, 886 (2017), [arXiv:1708.03491](#).
- P. Amaro-Seoane and et al., ArXiv e-prints (2017), [arXiv:1702.00786 \[astro-ph.IM\]](#).
- M. Charisi, I. Bartos, Z. Haiman, A. M. Price-Whelan, and S. Márka, *MNRAS* **454**, L21 (2015), [arXiv:1502.03113 \[astro-ph.HE\]](#).
- Y. Shen, Bulletin of the Astronomical Society of India **41**, 61 (2013), [arXiv:1302.2643 \[astro-ph.CO\]](#).
- D. J. D’Orazio, Z. Haiman, and D. Schiminovich, *Nature* **525**, 351 (2015b), [arXiv:1509.04301 \[astro-ph.HE\]](#).
- Planck Collaboration, P. A. R. Ade, N. Aghanim, M. Arnaud, M. Ashdown, J. Aumont, C. Baccigalupi, A. J. Banday, R. B. Barreiro, J. G. Bartlett, and et al., *A&A* **594**, A13 (2016), [arXiv:1502.01589](#).
- A. G. Riess, L. M. Macri, S. L. Hoffmann, D. Scolnic, S. Casertano, A. V. Filippenko, B. E. Tucker, M. J. Reid, D. O. Jones, J. M. Silverman, R. Chornock, P. Challis, W. Yuan, P. J. Brown, and R. J. Foley, *ApJ* **826**, 56 (2016), [arXiv:1604.01424](#).
- Z. Ivezić and et al., ArXiv e-prints (2008), [arXiv:0805.2366](#).
- S. G. Djorgovski et al., ArXiv e-prints (2011), [arXiv:1102.5004 \[astro-ph.IM\]](#).
- K. Schutz and C.-P. Ma, *MNRAS* **459**, 1737 (2016), [arXiv:1510.08472](#).
- B. F. Schutz, *Nature* (ISSN 0028-0836) **323**, 310 (1986).
- B. P. Abbott, R. Abbott, T. D. Abbott, F. Acernese, K. Ackley, C. Adams, T. Adams, P. Addesso, R. X. Adhikari, V. B. Adya, and et al., *Nature* **551**, 85 (2017), [arXiv:1710.05835](#).
- Z. Haiman, ArXiv e-prints (2017), [arXiv:1705.06765 \[astro-ph.HE\]](#).
- Z. Abraham and G. E. Romero, *A&A* **344**, 61 (1999).
- Z. Yuan, J. Wang, M. Zhou, L. Qin, and J. Mao, *ApJ* **846**, 78 (2017), [arXiv:1708.03087 \[astro-ph.HE\]](#).